Thèse présentée en vue de l'obtention du diplôme de

Doctorat LMD en Electronique

Spécialité**: Micro-électronique et Micro systèmes embarqués**

Thème

Etude par simulation numérique d'une cellule solaire tandem Pérovskite/Silicium.

Présentée par
Bacha Madjda

Soutenue publiquement le 20 / 12 / 2023

Devant le jury composé de :

Nom et Prénom	Grade	Etablissement	Qualité
Tibermacine Tofik	Professeur	Université de Biskra	Président
Saâdoune Achour	Professeur	Université de Biskra	Rapporteur
Dehimi Lakhdar	Professeur	Université de Batna	Examinateur
Bekhouche Khaled	M.C.A	Université de Biskra	Examinateur

Abstract

Solar cells have become a prominent solution for harnessing renewable energy, offering a clean and sustainable alternative to traditional power generation methods. Among various photovoltaic technologies, perovskite solar cells (PSCs) have gained significant attention due to their exceptional optoelectronic properties and rapid advancements in power conversion efficiency (PCE). Silicon is a most widely used photovoltaic material with high efficiency and stability, while perovskites offer high absorption coefficients, tunable bandgaps, and ease of fabrication. This combination allows for efficient harvesting of a broader range of the solar spectrum, resulting in enhanced overall performance. In this thesis, Perovskite/Silicon tandem solar cell has been modelled based on methylammonium mixed bromide-iodide lead perovskite using Silvaco Atlas simulator. Our work started by optimizing the single perovskite solar cell structure TiO_2/$CH_3NH_3PbI_{3-x}Br_x$/Spiro-OMeTAD, where the optimization were in particular on the different layer thicknesses of the cell and also on the carrier lifetime. The obtained results showed an enhancement in power conversion efficiency PCE of 24.72%. Secondly, we combine the perovskite top sub-cell with the SHJ bottom sub-cell to obtain more high efficiency of the tandem design. The results show PCE of 27.02% under mismatched current densities between top, bottom, and tandem cells. Finally, by achieving the current matching between the three cells, $J_{SC\ top} \simeq J_{SC\ bottom} \simeq J_{SC\ tandem} \simeq$ 18.80mA/cm^2, we enhanced the power conversion efficiency to 31.67%.

Keywords:

$CH_3NH_3PBI_{3-x}Br_x$, Perovskite, ETL, HTL, Silicon, PCE, Thickness, Current matching, Silvaco Software.

Résumée

Les cellules solaires sont devenues une solution prédominante pour exploiter les énergies renouvelables, offrant une alternative propre et durable aux méthodes traditionnelles de production d'énergie. Parmi les différentes technologies photovoltaïques, les cellules solaires à base de pérovskite (CSP) ont suscité une attention considérable en raison de leurs propriétés optoélectroniques exceptionnelles et de leurs progrès rapides en termes d'efficacité de conversion de l'énergie (PCE). Le silicium est un matériau photovoltaïque largement utilisé en raison de son efficacité et de sa stabilité élevée, tandis que les pérovskites offrent des coefficients d'absorption élevés, des bandes interdites ajustables et une facilité de fabrication. Cette combinaison permet une exploitation efficace d'une plus large gamme du spectre solaire, ce qui se traduit par une amélioration des performances globales. Dans cette thèse, une simulation d'une cellule solaire tandem pérovskite/silicium, basée sur une pérovskite de plomb bromure-iode mélangé de méthylammonium, $CH_3NH_3PbI_{3-x}Br_x$, et des structures à hétérojonction de silicium (SHJ), a été réalisée à l'aide du simulateur Silvaco Atlas. Notre travail a commencé par l'optimisation de la structure de la cellule solaire à pérovskite unique $TiO_2/CH_3NH_3PbI_{3-x}Br_x$/Spiro-OMeTAD, avec une optimisation en particulier sur les différentes épaisseurs de couche de la cellule et également sur la durée de vie des porteurs. Les résultats obtenus ont montré une amélioration de l'efficacité de conversion d'énergie (PCE) de 24,72 %. Deuxièmement, nous avons combiné la sous-cellule supérieure à pérovskite avec la sous-cellule inférieure en silicium pour obtenir une efficacité plus élevée de la conception en tandem. Les résultats montrent une PCE de 27,02 % en présence de densités de courant non assorties entre les cellules supérieure, inférieure et en tandem. Enfin, en atteignant une correspondance de courant entre les trois cellules, $J_{SC\ Sup} \simeq J_{SC\ Inf} \simeq J_{SC\ tandem} \simeq 18.80 mA/cm^2$, nous avons amélioré l'efficacité de conversion d'énergie de la cellule en tandem à 31,67 %.

Mots-clés :

Cellule solaire à pérovskite, CH3NH3PBI3-xBrx, Cellule solaire au silicium, PCE, Épaisseur, Adaptation de courant, Silvaco Atlas.

ملخص

أصبحت الخلايا الشمسية حلاً بارزًا لتسخير الطاقة المتجددة ، حيث تقدم بديلاً نظيفًا ومستدامًا لأساليب توليد الطاقة التقليدية. من بين العديد من التقنيات الكهروضوئية ، اكتسبت خلايا البيروفسكايت الشمسية (PSCs) اهتمامًا كبيرًا نظرًا لخصائصها الإلكترونية الضوئية الاستثنائية والتقدم السريع في كفاءة تحويل الطاقة (PCE) . السيليكون هو أكثر المواد الكهروضوئية استخدامًا بكفاءة واستقرار عاليين ، بينما توفر البيروفسكايت معاملات امتصاص عالية ، وفجوات نطاق قابلة للضبط ، وسهولة في التصنيع. يسمح هذا المزيج بالحصاد الفعال لمجموعة أوسع من الطيف الشمسي ، مما يؤدي إلى تحسين الأداء العام. في هذه الأطروحة ، تم إجراء محاكاة لخلية شمسية ترادفية من البيروفسكايت / السيليكون ، استنادًا إلى بيروفسكيت الرصاص بروميد يوديد الميثيل الأمونيوم المختلط $CH_3NH_3PbI_{3-x}Br_x$ ، وهياكل تقاطع السيليكون غير المتجانسة (SHJ) باستخدام جهاز المحاكاة Silvaco Atlas . بدأ عملنا من خلال تحسين بنية الخلية الشمسية المفردة من البيروفسكايت $TiO_2/CH_3NH_3PbI_{3-x}Br_x/Spiro\text{-}OMeTAD$ ، حيث كان التحسين على وجه الخصوص على سماكات الطبقات المختلفة في الخلية وكذلك على عمر حامل الشحنة. أظهرت النتائج التي تم الحصول عليها زيادة في كفاءة تحويل الطاقة PCE بنسبة 24.72٪. ثانيًا ، نقوم بدمج الخلية الفرعية العلوية من البيروفسكايت مع الخلية الفرعية السفلية من السيليكون للحصول على كفاءة عالية للتصميم الترادفي. تظهر النتائج أن كفاءة تحويل الطاقة (PCE) بنسبة 27.02٪ تحت كثافة تيار غير متطابقة بين الخلايا العلوية والسفلية والخلايا الترادفية. أخيرًا، من خلال تحقيق المطابقة في كثافة التيار بين الخلايا الثلاث، عززنا كفاءة تحويل الطاقة للخلية الترادفية إلى 31.67٪.

الكلمات المفتاحية :

الخلايا الشمسية، البيروفسكايت، السيليكون، سيلفاكو أطلس، مردود التحويل الطاقوي، سماكة.

Dedication

I dedicate this modest work to my beloved parents and my beloved

grandmother who have been my source of inspiration and strength, who

continually provide their moral, spiritual and emotional support.

To my sisters, brother, friends, relatives who shared words of advice and

encouragement to finish this thesis.

Special dedication to my husband, Imad Youcef, who has been a constant source

of support and for his patience with me.

To the biggest gift of my life, to my daughter Nada, who had taught me what it

means to love unconditionally.

To my dear aunt who left us, she was very generous and always smiling, may

God keep you in his vast paradise.

I say thank you

Acknowledgement

First of all, I thank Allah, the Almighty, who gave me the strength, patience and

will to accomplish this modest work.

Also, my thesis supervisor Pr. Achour Saâdoune,

for his supervision, his directives and his availability.

Also, I thank him for his encouragement and sympathy throughout the period of

preparing my work.

My thanks also go to the jury members, Professor Tibermacine Toufik, Dr.

Bekhouche Khaled, and Professor Dehimi Lakhdar for their presence and for

the time they were willing to devote to evaluating this work.

I also thank all the teachers of the electronics department of

Mohamed Khider Biskra University who participated in my training

throughout the university cycle.

TABLE OF CONTENTS

Chapter 3 : Simulation Software

LIST OF FIGURES

Chapter 3

Chapter 4

LIST OF TABLES

LIST OF ABBREVIATIONS AND SYMBOLS

Abbreviations

PVK Perovskite

PCE Power conversion efficiency

NREL National Renewable Energy Laboratory

PSCs Perovskite solar cells

DSSCS Dye-sensitized solar cells

OPVs Organic photovoltaic cells

ETL Electron transporting layer

HTL Hole transporting layer

ITO Indium tin oxide

Spiro-OMeTAD (2,2',7,7'-tetrakis(N,N-di-p-methoxyphenylamine)-9,9'-spirobifluorene)

PTAA Poly(triaryl amine)

PEDOT: PSS poly (3,4- ethylenedioxythiophene) polystyrene sulphonate

PCBM [6,6]-phenyl C_{61} butyric acid methyl ester

c-Si Crystalline silicon

a-Si Amorphous silicon

SHJ Silicon hetero-junction solar cell

TCOs Transparent conductive layers

Symbols

hv Photon energy

h Planck's constant

v frequency of the light wave

c Speed of light

λ Light wavelength

ρ Resistivity

σ Conductivity

E_F Fermi level

E_g Band gap Energy

VB Conduction band

CB Valance band

N_V Effective density of state in the valence band

N_C Effective density of state in the conduction band

n_i The intrinsic carrier concentration

n The concentration of free electrons

p The concentration of free holes

k Boltzmann's constant

T Absolute temperature

N_A Concentration of acceptors

N_D Concentration of donors

f**(E)** Fermi function (probability distribution function)

$\overrightarrow{J}_{drift}$ Drift current

q Elementary charge

$\vec{E}$ Electric field

μ_n Electron mobility

μ_p Hole mobility

$\vec{J}_{diffusion}$ Diffusion current

D_n Electron diffusion constant

D_p Hole diffusion constant

$\vec{V_n}$ Electron concentration gradient

$\vec{V_p}$ Hole concentration gradient

$\frac{\partial n}{\partial t}$ Carrier continuity equation for electrons

$\frac{\partial p}{\partial t}$ Carrier continuity equation for holes

G_n Generation rate for electrons

G_p Generation rate for hole

R_n Recombination rate for electron

R_n Recombination rate for holes

σ_n Capture cross section of electron

σ_p Capture cross section of hole

$v_{th\,e}$ Thermal velocity of electron

$v_{th\,h}$ Thermal velocity of hole

N_t Concentration of effect states

E_t Energy of defect state

I_L Light induced current

I_D Dark current

V The cell voltage

V_{OC} Maximum voltage at zero current

I_{SC} Short-circuit current (V=0)

FF Fill factor

V_{MP} Maximum power voltage

I_{MP} Maximum power current

P_{MAX} Maximum power

η Efficiency

Introduction

Introduction

Third-generation photovoltaic technology has become more prevalent in high power conversion efficiency (PCE) devices in the last ten years. The third generation of PV cells has been constructed using a variety of semiconductor materials, including the Copper Zinc Tin Sulphide (CZTS), Dye-Sensitized Solar Cells (DSSCs), Organic Solar Cell, Perovskite (PVK) Solar Cell (PSC), and Quantum Dot Solar Cell. The benefits of high PCE and low cost fabrication make research on single solar cell architectures very attractive [1-3]. However, the primary challenge with single junction cells is their efficiency limitation, known as the Shockley–Queisser limit. This issue can be avoided through the use of tandem solar cells or multi-junction cells, in which two or more separate cells are merged to effectively capture the full range of solar energy by using various band gaps. In this regard, tandem configurations consist of two structured sub-cells (top and bottom) designed to attain efficiencies over 25% [4, 5]. The top sub-cell, featuring a wide band gap absorber material, captures high-energy photons while for the bottom sub-cell, containing a narrow band gap absorber material, absorbs lower-energy photons. Additionally, in order to improve the cell performance, numerous research groups have integrated different sub-cell architectures, such as PVK/CIGS [6-8], PVK/PVK [9-12], PVK/Si [13-18], and many others.

Perovskite, in particular, has found extensive use in tandem solar cells due to its efficient conversion of ultraviolet and visible light when combined with low band gap semiconductors like crystalline silicon, which successfully converts infrared light [33-38], recently, it has emerged as a viable approach to achieve both cost-effectiveness and high PCE [1-3]. Beyond its use in photovoltaic (PV) applications, perovskite also holds considerable importance in various other applications, for instance, light-emitting diodes (LEDs) [4-7], thin-film transistors (TFTs), and light-emitting transistors (LETs) [8-10].

The indicated power conversion efficiency (PCE) of perovskite solar cell technology has garnered significant interest, witnessing a substantial increase from 3.8% in 2009 [11] to over 20% within a few years [12-18], thanks to their specific characteristics including high carrier diffusion lengths [19], band gap tunability [20-23], and high absorption coefficient [24,25].

 The majority of researchers have concentrated on methylammonium lead iodide ($CH_3NH_3PbI_3$, also known as $MAPbI_3$), which is positioned as the active layer sandwiched between two transport layers (ETL and HTL), which are electron and hole transport layers, respectively. This mostly employed structure, ETL/Perovskite absorber/HTL, is used with various ETLs such as PCBM and TiO2, as well as HTLs like spiro-OMeTAD and PEDOT:PSS [32-34].

In addition to the conventional pure perovskite, mixed-halide perovskite materials ($CH_3NH_3PbI_{3-x}Cl_x$, $CH_3NH_3PbCl_{3-x}$ or $CH_3NH_3PbI_{3-x}Br_x$) have also been utilized as light-absorbing materials. The incorporation of bromine Br into $CH_3NH_3PbI_3$ in these mixed-halide materials has proven effective in enhancing the devices stability, thereby improving the overall performance of perovskite devices [20, 35].

In this thesis, using Silvaco ATLAS simulator, we employed mixed halide perovskite $CH_3NH_3PbI_{3-x}Br_x$ as light absorbing material. Our objective is to enhance the PCE by optimizing the materials thickness of the used structure and enhancing the carrier lifetime within the absorber layer of the single perovskite solar cell, and also to study the effect of the top cell perovskite thickness on the behavior of PVK/Si tandem solar cell.

Chapter 1
Basic physics
of solar cells

1.1 Introduction

Solar cells represent a highly promising and potentially important technology, shaping the future of sustainable energy for humanity. The term solar cells, also known as photovoltaic cells, are devices that convert incident light directly into electrical energy using the photovoltaic effect. The first appearance in history for solar cells is in the 19th century. A solar cell is made up of a thin layer of semiconductor material, typically silicon that has been doped to create a p-n junction. When sunlight (particles of light) reaches the surface of a solar cell, the electrons in the material are excited, causing them to move around and generate an electric current. The more intense the sunlight, the more energy is produced by the solar cell.

This chapter discusses semiconductor and solar cell basics. We start by introducing some fundamental physics of semiconductors as energy band gap theory, generation and recombination of carriers, PN junction mechanism and other properties. And also the chapter presents the solar cell equivalent circuit and the essential extracted parameters of a solar cell with their equations.

1.2 Introduction to semiconductors

1.2.1 Basic physics

Materials may be divided into three classes based on their electrical characteristics and their ability to conduct an electric current (*conductors*, *semiconductors* and *insulators).*Where resistivity ρ and conductivity σ stand out as among the most crucial electrical properties. Figure 1.1 presents the resistivity and conductivity of different material types.
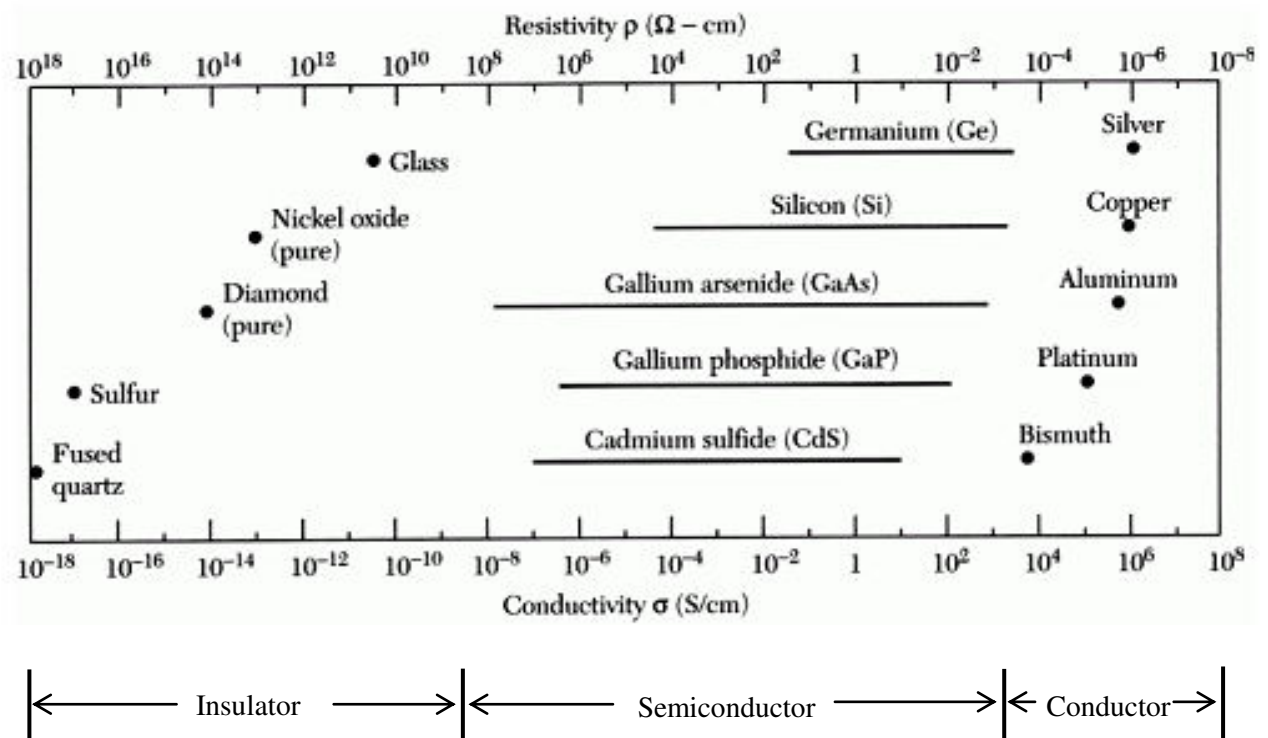
Figure 1.1: Different materials with their resistivity and conductivity [54].

Insulators: An insulator is a material that does not allow the flow of current. It has very high resistivity and very low conductivity.

Semiconductors: A semiconductor is a material with conductivity that falls between that of a conductor and an insulator. It has intermediate conductivity.

Conductors: A conductor is a material that permits flowing of the charge when a voltage is applied to it. Because the conductors have a high conductivity, they can easily conduct electrical current.

Figure 1.2 presents material classification based on energy band diagram, where, insulators are materials characterized by wider bandgaps, while conductors are materials without bandgaps or with negative band gaps. Semiconductors, on the other hand, occupy the intermediate position between conductors and insulators.

6
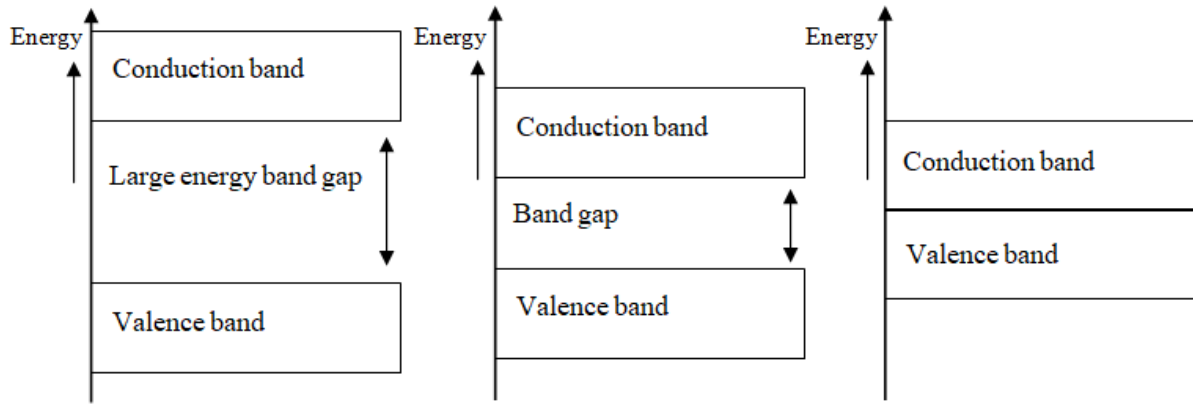
Figure 1.2: Material Classification based on Energy Band Diagram.

1.2.2 Energy band and energy gap theory

The theory of energy band is crucial in understanding how electrons respond to multiple conditions inside a crystal structure. These energy bands are made up of an upper energy band levels known as the conduction band CB, a lower band of energy level known as the valence band VB, and the bandgap, which is the energy gap between the two states [55]. The bandgap values of different elements vary, and these variations have a remarkable effect on the electrical characteristics of those elements.

The Fermi level (EF), which indicates the average energy level for electrons, can also be utilised in the band diagram. EF is often located in the middle of the bandgap in an intrinsic semiconductor. (Figure 1.3).
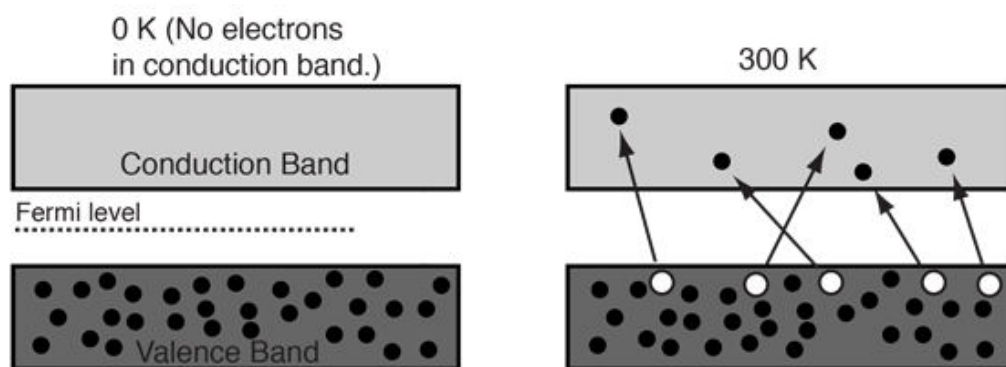
Figure 1.3:.Semiconductor energy band at 0 and 300 K.

From figure 1.3 Electrons tend to move towards lower energy states, and when a substance reaches absolute zero temperature (0 K), the valence band is entirely occupied by electrons, while the conduction band is entirely empty of electrons. And, if enough energy (300 K) is

provided to the electron at the top of the valence band, the electron may transit to the bottom of the conduction band. This transition results in the creation of a vacant electron state within the valence band, which is commonly referred to as a "hole."

1.2.3 Light absorption and carrier generation

Each semiconductor has an energy band gap E_g, where E_g is the amount of energy required to liberate an electron from the nucleus and hence produce one electron-hole pair. Light can be used to deliver this required energy. Each photon of light has the energy hv, where h indicates the Planck's constant and v indicates the frequency of the light wave. Whereas hv can be written as:

$$\text{hv (ev)} = h \frac{c}{\lambda} = \frac{1.24}{\lambda(\mu m)} \tag{1.1}$$

The equation provided calculates the energy of photons, where "c" represents the speed of light, and "λ" denotes the wavelength of the light. In semiconductors, the absorption of photons occurs when their energy (hv) exceeds the semiconductor's band gap (hv $> E_g$). When this happens, each absorbed photon elevates an electron from the VB to the CB, forming an electron-hole pair. Any surplus energy beyond this process is released as heat. Besides, photons with energy values lower than the band gap (hv $< E_g$) are not absorbed by the semiconductor and are unable to create electron-hole pairs.

1.2.4 Direct and indirect band gap

The band structure of a semiconductor describes the distribution of energy levels that electrons can occupy within the material. The valence band is the highest band of occupied electron energy levels, while the conduction band is the lowest band of unoccupied electron energy levels.

In a direct band gap semiconductor, the minimum energy level of the conduction band is directly above the maximum energy level of the valence band, with no energy level in between. This means that an electron can easily transition from the valence band to the conduction band by absorbing a photon of the appropriate energy. Direct band gap semiconductors are used in applications such as light-emitting diodes (LEDs) and lasers [56].

In contrast, in an indirect band gap semiconductor such as Si or Ge, there is an energy level between the valence and conduction bands. This makes it more difficult for an electron to the transition from the VB to the CB necessitates more than just photon absorption; it also involves the emission or absorption of a phonon. (a quantum of vibrational energy). Indirect band gap

semiconductors are less efficient at generating light, but are still used in applications such as solar cells [56].

a)　Direct band gap　　　　　　　　　　　b)　Indirect band gap
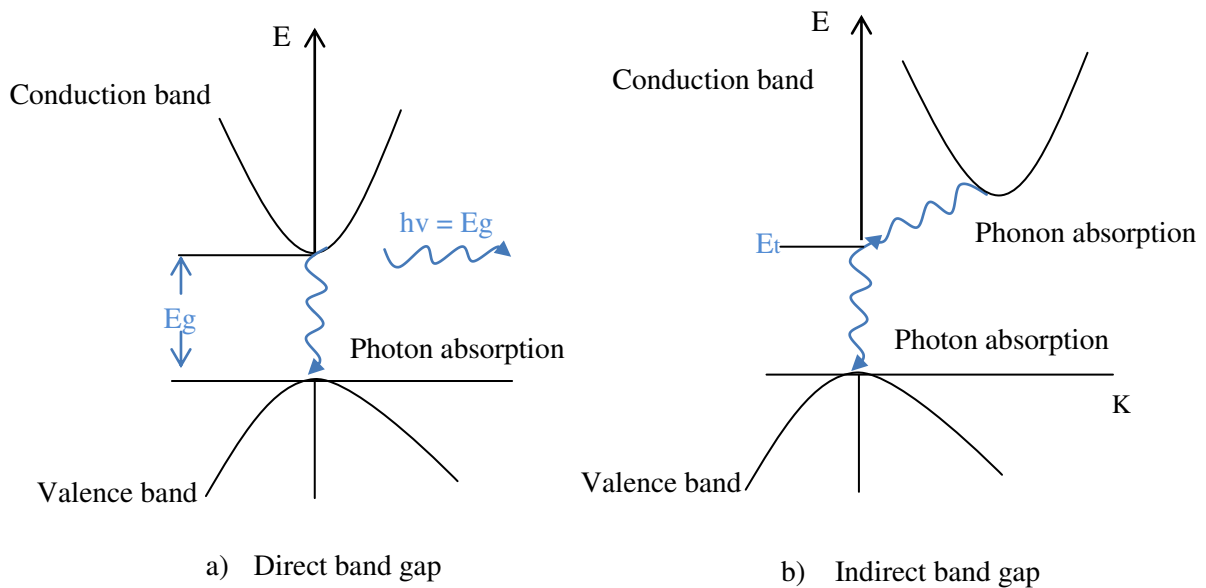
Figure 1.4: Drawing of direct and indirect band gaps semiconductors.

Perovskite materials can have either direct or indirect band gaps depending on their composition and structure.

In general, perovskites with a smaller lattice constant, such as CsPbBr3, tend to have a direct band gap, while those with a larger lattice constant, such as CH3NH3PbI3, tend to have an indirect E_g.

1.2.5 Fermi level

In semiconductors, the Fermi level refers to the energy level in the material's electronic band structure. At higher temperatures, electrons can move between energy levels due to thermal excitation, and the Fermi level can shift as a result.

The Fermi function, signified as $f(E)$, determines the occupancy of available states at energy level E with electrons. It can be described as a probability distribution function with the following definition:

$$f(E) = \frac{1}{1 + e^{\frac{E - E_F}{KT}}} \tag{1.2}$$

Where E is the electron energy, E_F is the Fermi level, k is Boltzmann's constant and T is the absolute temperature.

For intrinsic semiconductors (i.e., a pure semiconductor with no intentional doping) the Fermi level situated at the midpoint of the energy gap between the VB and the CB. At this point, the number of holes in the valence band equals the number of electrons in the conduction band of an intrinsic semiconductor. Hence we have:

$$n = p = n_i \tag{1.3}$$

$$\text{or} \quad np = n_i^2 \tag{1.4}$$

Where:

n, p: the concentrations of free electrons and holes, respectively.

n_i: the intrinsic carrier concentration.

$$n = N_C exp\left(-\frac{E_c - E_F}{KT}\right) \tag{1.5}$$

$$p = N_V exp\left(-\frac{E_F - E_V}{KT}\right) \tag{1.6}$$

Where:

N_c, N_V are the effective densities of states in the CB and VB, respectively.

Then, using n=p=n_i, we can write from equations (1.5) and (1.6):

$$N_C exp\left(-\frac{E_c - E_F}{KT}\right) = N_V exp\left(\frac{E_V - E_F}{KT}\right) \tag{1.7}$$

Solving the equation (1.7) for E_F, we get the expression:

$$E_i = E_F = \frac{E_C + E_V}{2} - \frac{KT}{2} ln\left(\frac{N_C}{N_V}\right) \tag{1.8}$$

$$\underline{\hspace{6cm}} \quad E_C$$

$$E_F \quad \text{-----------------------------------} \quad E_i$$

$$\underline{\hspace{6cm}} \quad E_V$$
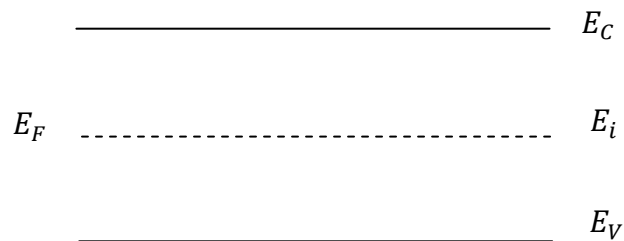
Figure 1.5: Fermi level for intrinsic semiconductor [57]

In a doped semiconductor (extrinsic semiconductors), the Fermi level can shift closer to the energy level of the majority carrier (i.e., electrons in an n-type semiconductor or holes in a p-

type semiconductor). This shift creates a gradient in the electron concentration that drives the flow of charge carriers and makes the semiconductor useful for electronic devices.

Condition of neutrality has to be followed. For example, if there are one type of donors and one type of acceptors: $p + N_D^+ = n + N_A^-$

For n-type semiconductor, $N_D \gg N_A$, hence, $N_D = n$, and from the expression (1.5)

$$n = N_c \exp\left(-\frac{E_C - E_F}{KT}\right) \tag{1.9}$$

$$N_D = N_c \exp\left(-\frac{E_C - E_F}{KT}\right) \tag{1.10}$$

So that, the Fermi level can be defined as:

$$E_C - E_F = KT \ \ln\left(\frac{N_C}{N_D}\right) \tag{1.11}$$

$$
\begin{array}{ll}
\rule{7cm}{0.4pt} & E_C \\
\rule{7cm}{0.4pt} & E_F \\
\text{-------------------------------------} & E_i \\
\\
\rule{7cm}{0.4pt} & E_V
\end{array}
$$
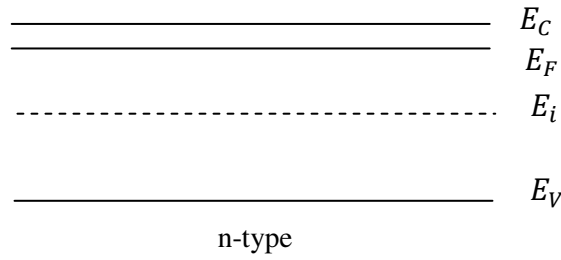
<div align="center">n-type</div>

Figure 1.6: N- type semiconductor Fermi level position [57].

For p-type semiconductor, $N_A \gg N_D$, hence, $N_A = p$, and from the expression (1.6)

$$p = N_V \ \exp\left(\frac{E_V - E_F}{KT}\right) \tag{1.12}$$

$$N_A = N_V \exp\left(\frac{E_V - E_F}{KT}\right) \tag{1.13}$$

So that, the Fermi level can be defined as:

$$E_F - E_V = KT \ \ln\left(\frac{N_V}{N_A}\right) \tag{1.14}$$

$$E_C$$

$$E_i$$

$$E_F$$

$$E_V$$
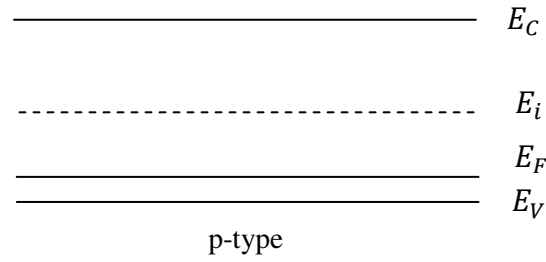
p-type

Figure 1.7: P-type semiconductor Fermi level position [57].

1.2.6 Carrier transport

In semiconductor devices, including *pn* junctions, carrier transport can be described by the following equations.

Poisson's equation:

In a semiconductor doped by the two types of dopants, the concentration of total charges takes into account free carriers and atoms or ionized impurities:

$$\rho = e \, (N_D^+ - \ N_A^- + p - n) \tag{1.15}$$

At room temperature all donors and acceptors are ionized so that the space charge is simply written:

$$\rho = e \, (N_D - \ N_A + p - n) \tag{1.16}$$

Carrier drift and diffusion:

Drift and diffusion of electrons and holes are responsible for generating electric current in semiconductors. Drift current is the movement of charge carriers caused by the applied electric field. Charged particles are swept by the applied electric field. Electrons having negative charges are swept in the opposite direction of the field while holes having positive charges are swept in the same direction as the field, resulting in an electric current which by convention is in the same direction as the electric field. Drift current which depends on the applied electric field and is proportional to the conductivity of electrons and holes is given by:

$$\overrightarrow{J}_{n,drift} = q\mu_n n\vec{E} \tag{1.17}$$

$$\overrightarrow{J}_{p,drift} = q\mu_p n\vec{E} \tag{1.18}$$

Where q indicates the elementary charge, $\vec{E}$ expressed the electric field and μ_n and μ_p are electron and hole mobility, respectively.

Diffusion current is the current which is due to the motion of charge carriers occurring because of non-uniform distribution of electrons and holes in a semiconductor. It can be either in the same or opposite direction of a drift current. Electron and hole diffusion currents depending on the gradient of the carrier concentration are:

$$\vec{J}_{n,diffusion} = qD_n\vec{V_n} \tag{1.19}$$

$$\vec{J}_{p,diffusion} = qD_pn\vec{V_P} \tag{1.20}$$

With D_n, D_p, $\vec{V_n}$, and $\vec{V_P}$ being electron diffusion constant, hole diffusion constant, electron concentration gradient and hole concentration gradient, respectively

The total current density of electrons and holes known as Drift-Diffusion equations can therefore be written as followsn:

$$\vec{J_n} = q\mu_n n\vec{E} + qD_n\vec{V_n} \tag{1.21}$$

$$\vec{J_p} = q\mu_p n\vec{E} + qD_p\vec{V_p} \tag{1.22}$$

Carrier continuity equations:

In semiconductors, the continuity equations are used to describe the behaviour of charge carriers (i.e., electrons and holes) in the material. These equations are a set of partial differential equations that express the conservation of charge carriers in time and space.

The continuity equations for electrons and holes in a semiconductor are given by:

$$\frac{\partial n}{\partial t} = \frac{1}{q}\vec{V}.\vec{J_n} + G_n - R_n \tag{1.23}$$

$$\frac{\partial p}{\partial t} = -\frac{1}{q}\vec{V}.\vec{J_p} + G_p - R_p \tag{1.24}$$

Where:

n and p are electron and hole densities, respectively. t is time. $\vec{J_n}$ and $\vec{J_p}$ are the electron and hole current densities, respectively. G_n, G_p. R_n and R_p are Generation and Recombination rates for electrons and holes, respectively.

1.2.7 Generation / Recombination

Generation is the process through which carriers are formed; in this regard, semiconductors absorb and transform light into electricity. The absorption rate depends upon two things: absorption coefficient, α (expresses absorption capability) and the thickness of the material. If light of intensity I_0 falls on a solar cell top surface, the intensity of light at any distance x is given by:

$$I = I_0 e^{-\alpha x} \tag{1.25}$$

The absorption coefficient of a material α is given by the following relationship:

$$\alpha = \frac{4\pi k}{\lambda} \tag{1.26}$$

The equation reveals that the absorption coefficient of a material changes depending on the wavelength, λ. This implies that a semiconductor material might effectively absorb light within a specific range of wavelengths.
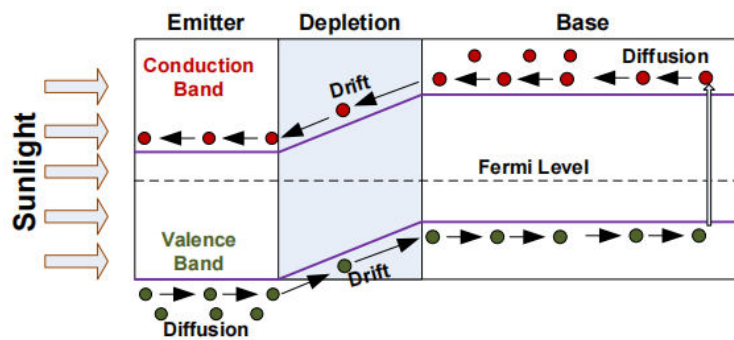
Figure 1.8: Light absorption and carrier transport [58].

As illustrated in figure 2.7, when a photon with sufficiently high energy (i.e., sufficiently low wavelength) interacts with an electron in the valence band, it elevates the electron to the conduction band, creating an empty hole in the valence band. This process generates an electron-hole pair in the base and emitter regions, respectively. The minority carriers in the p-type base and n-type emitter diffuse toward the depletion region. Upon entering the depletion region, they undergo drift due to the built-in electric field. Electrons formed in the base region drift toward the emitter region, and holes created in the emitter regions drift toward the base region. This movement of minority carriers induces a potential difference, leading to the splitting of the Fermi level, E_F, into minority electron quasi Fermi level, E_{FN}, and minority hole quasi Fermi level, E_{FP}[58].

Recombination is the process where the carriers are eliminated by combining. During recombination, every excess in energy the electron had is released. Once the electron and hole recombine and restore equilibrium, recombination is complete. During this process, A minor quantity of energy is emitted, which can be categorized as either radiative (emission of light "photon"), non-radiative (emission of heat "phonon"), or Auger (excess energy of charge carriers in a semiconductor is transferred to another charge carrier).

Band-to-band recombination takes place when an electron in the CB combines with a hole in the VB without changing its momentum [59].Usually, in direct band gap semiconductors, band-to-band recombination occurs by radiative transition.

Trap-assisted recombination (commonly referred as "Shockley-Read-Hall" or SRH recombination) occurs when an electron reaches a trap, or an energy level within the band gap induced by a structural defect or impurity. Finally, the electron takes a second step and returns to the valence band, where it recombines with a hole.
The equation determines the Shockley-Read-Hall recombination rate

$$U_{SRH} = \frac{pn - n_i^2}{c_{n0}(p + p_1) + c_{p0}(n + n_1)} \tag{1.27}$$

Where:

$$c_{n0} = \frac{1}{v_{th\,e}.\sigma_n.N_t} c_{p0} = \frac{1}{v_{th\,h}.\sigma_n.N_t} \tag{1.28}$$

And:

$$n_1 = n_i exp\left(\frac{E_t - E_i}{KT}\right) p_1 = n_i exp\left(\frac{E_i - E_t}{KT}\right) \tag{1.29}$$

and where σ_n and σ_p are capture cross sections of electrons and holes, $v_{th\,e}$ and $v_{th\,h}$ are the thermal velocities of +electrons and holes, N_t is the concentration of defect states, and E_t is the energy of the defect state [60].

Augur recombination needs three particles: at least one electron and one hole, with the third particle being either an electron or a hole. This sort of recombination is comparable to band-to-band recombination; nevertheless, the energy is transported to a third particle.
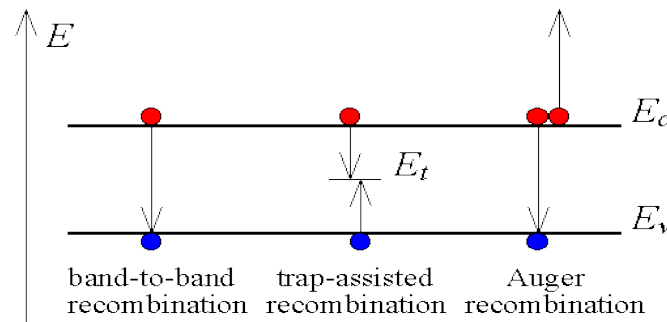
Figure 1.9: Types of recombination [59].

1.2.8 PN junction

Doped semiconductors have no charge and no diffusion current at equilibrium. PN junction refers to a semiconductor junction by joining two types, P-type and N-type. As they come into touch with one another, a number of phenomena are observed.

P-N Junction under Forward Bias

A p-n junction is a type of semiconductor junction formed by the contact of a p-type and an n-type semiconductor material. When a forward bias voltage is applied across a p-n junction, the positive terminal of the voltage source is connected to the p-type material and the negative terminal is connected to the n-type material. This causes the potential barrier at the junction to decrease, allowing current to flow across the junction more easily.

In a p-n junction diode, the forward bias voltage causes a significant increase in the current flowing through the diode. This is because the forward bias voltage reduces the width of the *depletion region* at the junction, allowing more electrons and holes to cross the junction and recombine, thus increasing the current flow.
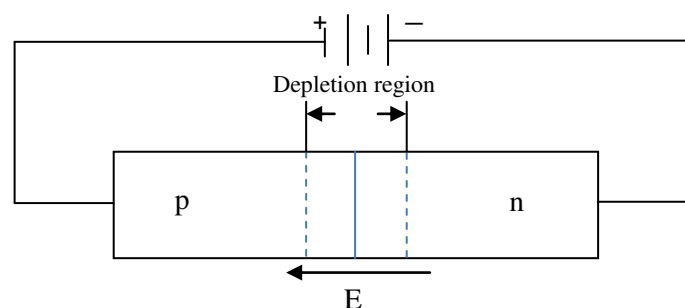
Figure 1.10: Forward bias for PN junction.

P-N Junction under Reverse Bias

In a reverse-biased p-n junction, the depletion region at the junction widens, resulting in a rise in the potential barrier. This prevents the majority carriers (electrons and holes in the n-type and p-type material, respectively) from crossing the junction, and as a result, only a very small amount of reverse leakage current flows.
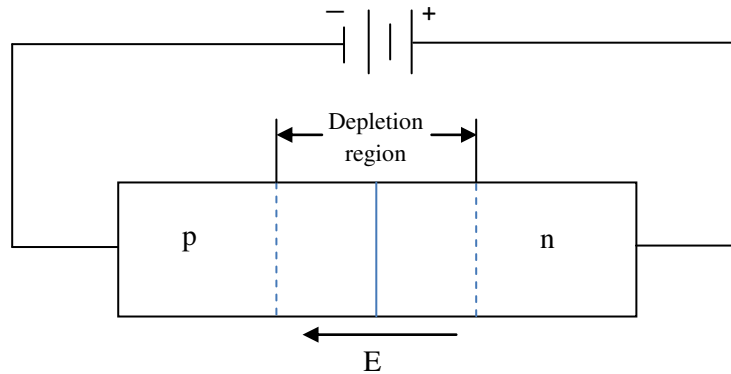
Figure 1.11: Reverse bias for PN junction.

I-V characteristics curve of a semiconductor diode

A semiconductor diode's V-I characteristics curve is shown below. This characteristic curve is a typical description for a semiconductor diode's V-I characteristic. When the current in the semiconductor diode crosses the forward voltage threshold, the diode begins to conduct.
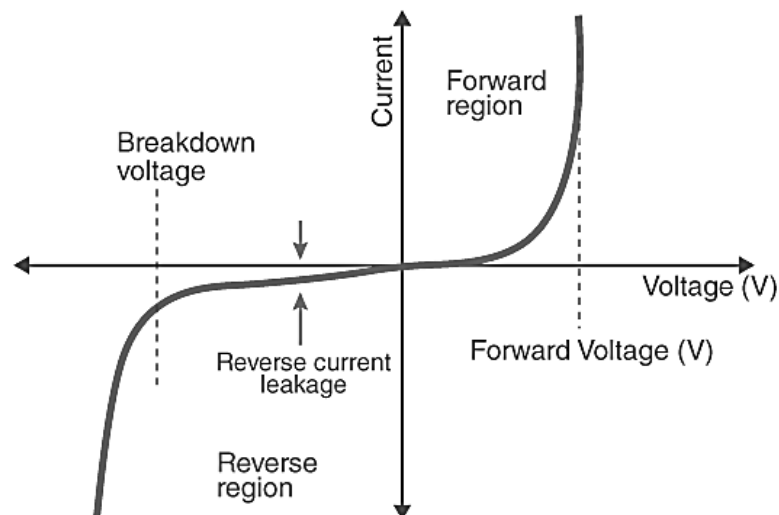
Figure 1.12: Forward & Reverse Bias I-V Characteristics of PN diode.

1.3 Solar cell fundamentals

1.3.1 Equivalent circuit

Using electric circuit design, the p-n junction of a solar cell could be represented as a diode.
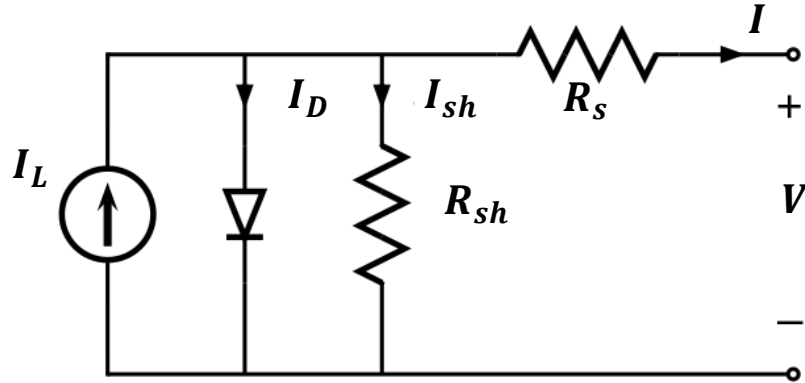
Figure 1.13: Solar cell equivalent circuit.

When element in the dark, the current I_D is transmitted through the diode. The net current I is the difference between the light-induced current (I_L) and diode current (I_D) and shunt current (I_{sh}):

$$I = I_L - I_D - I_{sh} \tag{1.30}$$

$$I = I_L - I_{sc}\left[exp\left(\frac{q(V+R_sI)}{aKT}\right) - 1\right] - \frac{V+R_sI}{R_{sh}} \tag{1.31}$$

Whereas

V= Voltage of the cell [V].

q = Electron charge.

k = Boltzmann constant.

T = absolute temperature [°K].

I_{sc} = Saturation current of the diode [A].

R_s = Series resistance.

R_{sh} = Shunt resistance.

a = Ideality Factor.

This is the basic equation explaining the relationship between voltage and current in a solar cell. If we plot cell voltage versus current (or current density), we get the curve of IV characteristics for solar cells shown below.
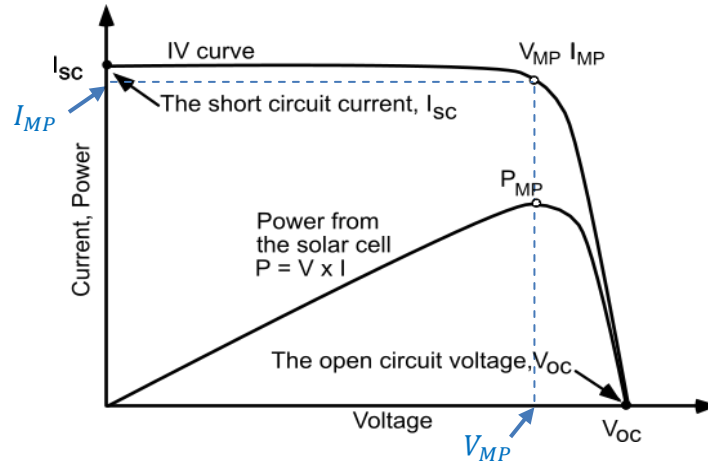
Figure 1.14: solar cell IV and power curves.

1.3.2 Electrical output parameters

From figure (1.13), there are several points of interest. Open Circuit Voltage V_{OC}, Short Circuit Current I_{SC} , Fill Factor FF and Power Conversion Efficiency PCE (η). These electrical parameters are key characteristics that determine its performance and efficiency.

Open circuit voltage

V_{OC} is the maximum voltage that a solar cell can generate at zero current. V_{OC} equation is given by:

$$V_{OC} = \frac{KT}{q} \ln \left(\frac{I_L}{I_D} + 1 \right) \tag{1.32}$$

Short circuit current

Similarly, when the cell is operated at short circuit, $V = 0$ and the current I through the terminals is defined as the short-circuit current I_{SC}. I_{SC} is determined by several factors, such as the type of semiconductor material used in the solar cell, the area of the cell, and the intensity of the incident light. Generally, higher intensity light will result in a higher short circuit current. In an ideal case, the short-circuit current is equal to light-induced current: $I_{SC} = I_L$.

Fill Factor

The fill factor (FF) is a parameter that describes the electrical performance of a solar cell, and it is defined as the ratio of the maximum power output of the cell. From curve (Figure 1.13), when the power reaches its maximum, the IV characteristic that correspond to that point are defined as maximum power voltage (V_{MP}) and current (I_{MP}): $P_{MAX} = I_{MP}V_{MP}$.

Therefore, the fill factor FF can be calculated as follows from the cell behaviours parameters:

$$FF = \frac{I_{MP}V_{MP}}{I_{SC}V_{OC}} \tag{1.33}$$

The fill factor can range from 0 to 1, with values closer to 1 indicating better performance. A typical fill factor for a commercial silicon solar cell is around 0.75 (75%).

Power conversion efficiency

Power conversion efficiency PCE is a measure of how effectively a solar cell can convert sunlight into usable electrical energy. A higher PCE indicates that a larger proportion of the incident solar energy is being converted into electrical energy.

$$PCE = \frac{P_{MAX}}{P_{in}} = \frac{I_{MP}V_{MP}}{P_{in}} = FF\frac{I_{SC}V_{OC}}{P_{in}} \tag{1.34}$$

Where P_{in}= input power

4.4 Conclusion

Semiconductors are a key component of solar cells. This chapter summarizes the main properties of a semiconductor. Where it can be classified in two types: intrinsic and extrinsic (n-type and p-type) semiconductor. Another two basic types of photovoltaic materials are direct and indirect band gap. The recombination process is much more efficient for a direct band gap semiconductors (which have strong optical transition) than for an indirect band gap semiconductor. A solar cell is the device that directly converts the absorbed sunlight energy into electricity through the process of photovoltaic; it is created by forming an electrical circuit with a PN junction. The basic characteristics of a solar cell are the short-circuit current (I_{SC}), the open-circuit voltage (V_{OC}), the fill factor (FF) and the solar energy conversion efficiency.

Chapter 2
Multijunction Solar cells

2.1 Introduction

Multijunction solar cells are a type of advanced photovoltaic technology that enables high-efficiency solar energy conversion by utilizing multiple semiconductor layers with different bandgap energies. These cells are designed to overcome the limitations of traditional single-junction solar cells. The idea of using multiple junctions to increase the efficiency of solar cells was proposed by American physicist William Shockley in 1956.

In the 1960s and 1970s, a number of researchers explored the potential of multijunction solar cells. One notable example was the work of American engineer Elliot Berman, who designed a multijunction solar cell with three layers of semiconductors in 1976. The cell was made of indium gallium arsenide (InGaAs), indium gallium phosphide (InGaP), and gallium arsenide (GaAs) layers, and achieved a conversion efficiency of 12.2%.

In the following decades, researchers continued to improve the efficiency of multijunction solar cells by optimizing the semiconductor materials and the device structure. In 1989, a research team at the National Renewable Energy Laboratory (NREL) led by Jerry Olson and Sarah Kurtz achieved a record-breaking efficiency of 35.9% for a multijunction solar cell consisting of three layers of semiconductors.

Various semiconductor materials are used in multijunction solar cells, such as gallium arsenide (GaAs), indium gallium phosphide (InGaP), perovskite and silicon (Si). The selection of materials depends on their bandgap energies and compatibility with the fabrication process. The layers are typically stacked on top of one another, allowing each layer to absorb the transmitted light from the preceding layers.

In this chapter we paid the attention to tandem architectures especially to the Perovskite/Silicon tandem structure. Where, firstly we gave generalities on perovskite solar cells (Crystal and solar cell structure). Secondly, we discussed the advantages of using silicon solar cell as a bottom cell. Finally, we present the Perovskite/Silicon tandem solar cell design with recent studies and efficiency records.

2.2 Generality on multijunction cells

2.2.1 The concept

As shown in Figure 2.1, Multijunction solar cells are advanced solar cells that consist of multiple p-n junctions made from different semiconductor materials stacked on top of each other. Each junction is optimized to absorb a specific range of the solar spectrum, allowing for higher energy conversion efficiency than single-junction solar cells.

In this context of single-junction solar cells structures, the theoretical efficiency limit is known as the Shockley-Queisser limit, named after the two researchers who derived it in 1961. The limit is based on the fundamental physical properties of semiconductors and the solar spectrum. the main issue of limiting their performance are the intrinsic losses of the combination of the single cell; where these losses refer to the losses of energy that occur within the cell itself, without any external factors affecting it. There are several intrinsic losses that can occur in a solar cell:

- *Recombination losses*: In this process, the electrons and holes that are generated by the absorption of light in the solar cell recombine before they can be extracted as electrical energy. This results in a loss of potential energy and reduces the efficiency of the solar cell.

- *Reflection losses*: Some of the light that falls on the surface of the solar cell is reflected back into the atmosphere. This reduces the amount of light that is available for absorption in the cell and decreases the overall efficiency of the cell.

- *Resistive losses*: The flow of electrical current in the solar cell encounters resistance from the material it passes through. This resistance results in the conversion of some of the electrical energy into heat, which is lost from the system.

- *Thermal losses*: When the solar cell absorbs light and converts it into electrical energy, it also generates some heat. If this heat is not removed efficiently, it can reduce the efficiency of the cell.

- *Auger recombination losses*: In this process, some of the excess energy from the recombination of electrons and holes is transferred to another free electron, which can cause it to recombine as well. This results in a loss of potential energy and a decrease in the efficiency of the solar cell.

Reducing these intrinsic losses is essential for improving the efficiency of solar cells and hence the cell performance.
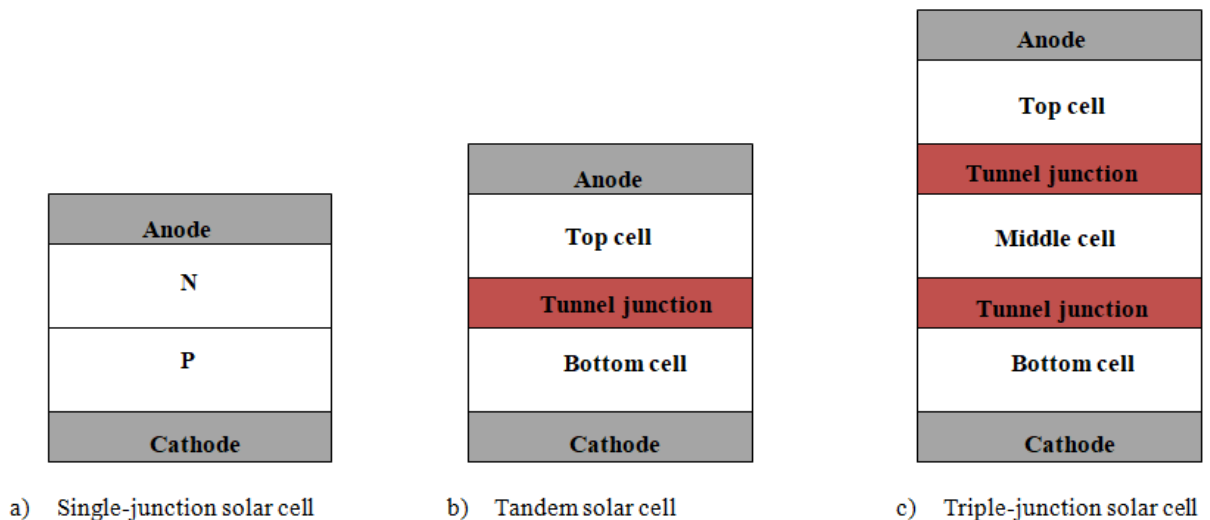
Figure 2.1: Solar cell designs for a) single-junction, b) Tandem, c) Triple-junction.

2.3 Evolution of solar cells

The evolution in this field can be traced back to the mid-19th century, when French physicist Alexandre-Edmond Becquerel discovered the photovoltaic effect, which is the basic physical process behind the operation of solar cells.

However, it wasn't until the 1950s that the first practical solar cell was developed. This ***first generation*** of solar cells, known as crystalline silicon solar cells, used highly purified silicon as the material to absorb the sunlight and generate electricity. The efficiency of these early solar cells was around 4%.

Over the following decades, researchers made significant advances in solar cell technology, developing new materials and manufacturing techniques that improved the efficiency of solar cells. In the 1970s, ***the second generation*** of solar cells was developed, which used thin film materials like amorphous silicon and cadmium telluride instead of crystalline silicon. These solar cells were cheaper to manufacture than their predecessors, but still had relatively low efficiency.

The third generation of solar cells, developed in the 1990s, included a variety of new materials and designs, including dye-sensitized solar cells (DSSCs), Organic photovoltaic cells (OPVs), Quantum dot solar cells and Perovskite solar cells. These solar cells had higher efficiency and were more flexible and lightweight than earlier generations, making them suitable for a wider range of applications.
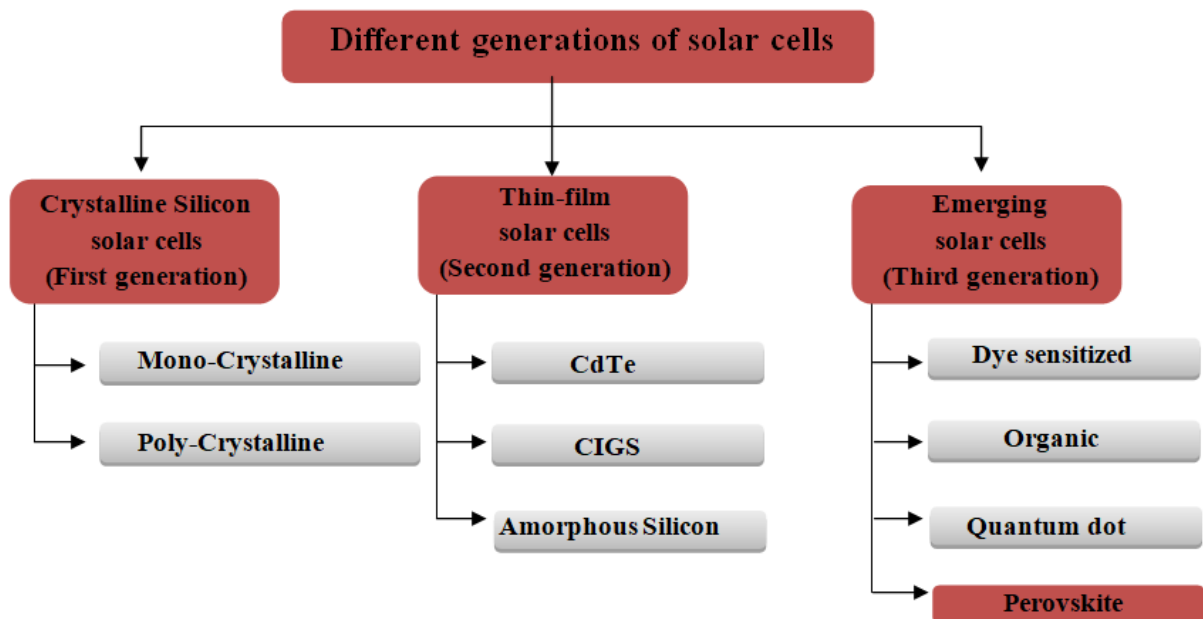
Figure 2.2: Solar cells three generations with photovoltaic materials.

2.4 Perovskite solar cells

2.4.1 Crystal structure

Perovskite is a general term referring to a class of materials with chemical formula of ABX3, where A and B are cations, and X is an anion.

This structure is named after the mineral perovskite, which has the chemical formula CaTiO3. However, many materials with the perovskite structure do not contain calcium or titanium. For example, as illustrated in Figure 2.3. The A-site is filled with cations such as methylammonium, $CH3NH3$ (MA), formamidinium, $[R_2N - CH = NR2]^+$ (FA), or Cs, either alone or mixed. The B-site contains the metal element, usually Pb, Sn or a mix of both. And the X-site has the halide elements, *e.g.* I, Br, Cl, or could be mixed halide [61].
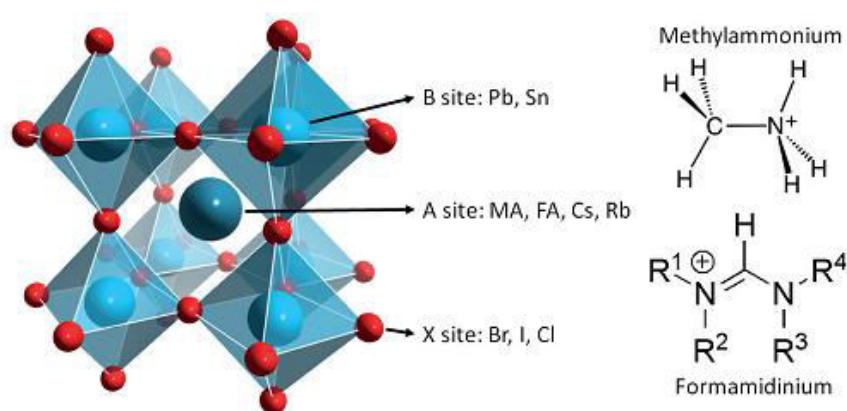
Figure 2.3: Perovskite crystal structure and chemical composition of the

two commonly utilised A-site cations.[61]

2.4.2 Solar cell structure

As presented in figure bellow, the fundamental structure of a PVK solar cell comprises of an active layer, an electron transporting layer (ETL), a hole transporting layer (HTL), and electrodes.
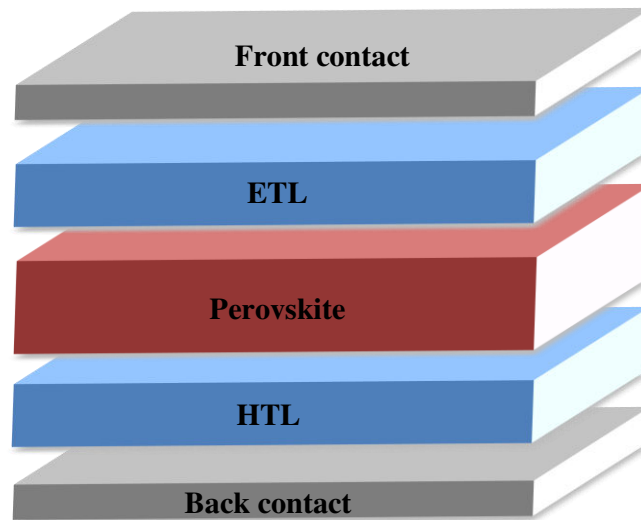
Figure 2.4: PSC general structure.

2.4.2.1 Perovskite active layer: types and overview

Perovskite materials can be broadly classified into two categories: inorganic perovskites and organic-inorganic hybrid perovskites. Here are some types of perovskite materials in each category:

Inorganic perovskites:

- Calcium titanate ($CaTiO_3$)
- Strontium titanate ($SrTiO_3$)
- Barium titanate ($BaTiO_3$)
- Lead zirconate titanate ($Pb(Zr,Ti)O_3$)
- Lanthanum aluminate ($LaAlO_3$)

Organic-inorganic hybrid perovskites:

- Methylammonium lead iodide ($CH_3NH_3PbI_3$)
- Formamidinium lead iodide ($HC(NH_2)_2PbI_3$)
- Cesium lead iodide ($CsPbI_3$)
- Methylammonium lead bromide ($CH_3NH_3PbBr_3$)
- Formamidinium lead bromide ($HC(NH_2)_2PbBr_3$)
- Methylammonium lead iodide bromide ($CH_3NH_3PbI_{1-x}Br_x$)

In perovskite solar cells, Perovskite mixed halides that contain a mixture of different halides, such as iodine (I), bromine (Br), or chlorine (Cl), in their crystal structure (for example $CH_3NH_3PbI_{1-x}Br_x$) can lead to tunable optical properties and bandgaps, which can be beneficial for improving the performance of perovskite solar cells. For example, mixed halide perovskites can have increased stability and reduced defect density compared to their single-halide counterparts, leading to improved power conversion efficiencies [62, 63].

2.4.2.2 ETL materials

In PVK cells, the primary role of ETL in PSCs is to harvest and transport photogenerated electrons while preventing recombination of carriers at the interface. Additionally, ETL directly influences the device's performance and stability. The following characteristics should be met by suitable electronic layer materials: 1) Demonstrating good electron mobility to ensure efficient electron transmission from the perovskite layer to the electrode, 2) Exhibiting high optical transmittance to minimize energy losses, 3) Possessing appropriate energy-level alignment to facilitate electron transfer and block hole migration [65].

Up to now, metal oxides such as titanium dioxide TiO_2, zinc oxide ZnO, tin oxide SnO_2 and other metal oxide materials are frequently utilized materials used in PSCs, owing to their exceptional properties, including high electron mobility and good energy level structure [64]. Typically, these materials are placed onto the active layer of a solar cell using processes such as spin-coating or vapour deposition.

2.4.2.3. HTL materials

In perovskite solar cells, a Hole Transport Layer (HTL) is an important component that makes transportation easier of holes from the perovskite layer to the electrode. The HTL is typically deposited on top of the transparent electrode, such as indium tin oxide (ITO), and plays a crucial role in preventing the recombination of charge carriers. When a hole is transported from the perovskite layer to the electrode, it can recombine with an electron, resulting in a loss of energy and a reduction in the efficiency of the solar cell. The HTL can act as a barrier to prevent this recombination by blocking the movement of electrons from the electrode into the perovskite layer [65].

Commonly used HTL materials in perovskite solar cells include Spiro-OMeTAD (2,2',7,7'-tetrakis(N,N-di-p-methoxyphenylamine)-9,9'-spirobifluorene) and Poly(triaryl amine) (PTAA).

These materials have high hole mobility and good stability, which makes them suitable for use in perovskite solar cells [66].

Figure 2.5 presents the energy levels for various representative materials of the most common PSCs.
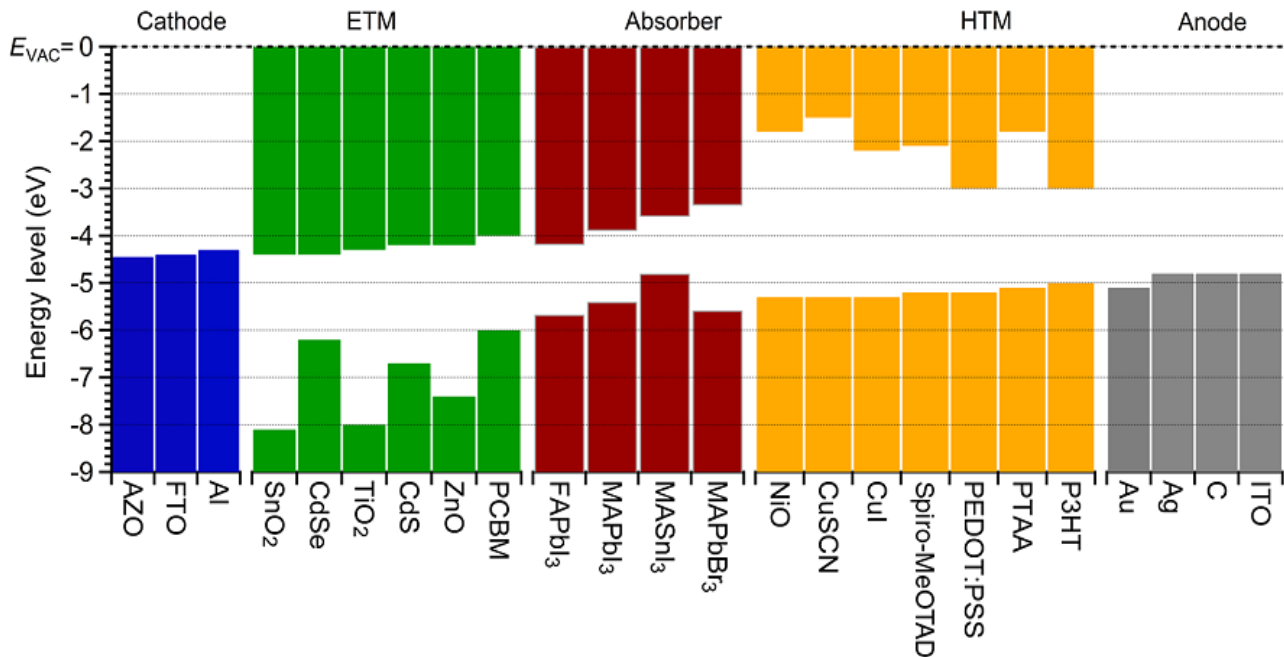
Figure 2.5: Energy levels diagram of different materials: ETLs, absorber and HTLs [67].

2.4.3 Classification of PSC structure

PVK solar cells can categorised as either regular n-i-p structure or inverted p-i-n structure, based on which transport material on the perovskite's exterior absorbs light.

- **Regular n-i-p structure of PSCs**

  Regular PSCs are further subdivided into planar and hetero-structured (mesoporous) PSCs, which exhibited the original concept of solid state dye sensitised solar cells (ssDSSCs). The regular type PSCs consist of n-type metal oxide blocking layer (BL), perovskite material, and hole transport materials (HTM) like spiro-OMeTAD (2,2′,7,7′-tetrakis-(*N*,*N*-di-4-methoxyphenylamino)-9,9′-spirobifluorene), PTAA [bis(4-phenyl) (2,4,6 rimethylphenyl)amine], P3HT (poly(3-hexylthiophene2,5-diyl) , CuSCN and CuI, and electrodes . [68]

- **Inverted p-i-n structure of PSCs**

In the context of inverted p-i-n type Perovskite Solar Cells (PSCs), the configuration includes poly(3,4-ethylenedioxythiophene) polystyrene sulphonate (PEDOT:PSS) serving as a promising hole transport layer (HTL), while [6,6]-phenyl C61 butyric acid methyl ester (PCBM), C60 are utilized as n-type electron transport layers (ETLs) [65]. It was Jeng et al. [37] who initially presented the concept of inverted PSCs, employing PEDOT:PSS as the HTL and PCBM as the ETL. These ETLs and HTLs also enable the construction of a mesoscopic p-i-n device structure. The most efficient mesoscopic p-i-n device, incorporating a nanostructured NiO film, achieved an impressive efficiency of 17.3%.

Figure bellow illustrated the planar n-i-p configuration (a) and the mesoporous n-i-p configuration (b).
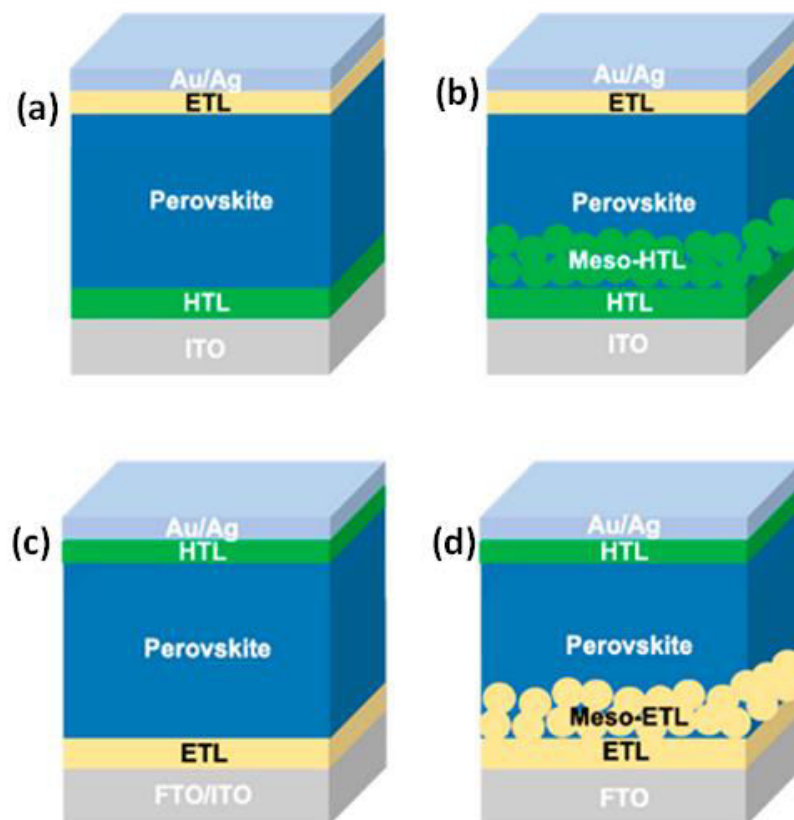
Figure 2.6: PSCs architectres of: a) planar n-i-p, b) mesoporouus n-i-p, c) Inverted p-i-n planar and d) inverted p-i-n mesoporous [69].

2.4.4 Properties of perovskite materials: advantages and characteristics

Perovskite cell devices have gained great attention in recent years due to their high power conversion efficiency, low-cost, and ease of manufacturing. Here are some of the advantages of perovskite solar cells:

1. High PCE: PSCs have reached (PCE) exceeding 25.5% in lab conditions, which is higher than other thin-film solar cells such as amorphous silicon (10-12%) and CdTe (22.1%) [70].

2. Low-cost: The materials used in perovskite solar cells are low-cost and abundant, making them an attractive alternative to traditional silicon-based solar cells. Additionally, the manufacturing process for perovskite solar cells is relatively simple and can be done at lower temperatures compared to silicon-based cells [71].

3. Tunable bandgap: By varying the compositiosn of the perovskite material, the bandgap of perovskite solar cells can be tuned. This means that perovskite solar cells can be optimized for different applications, such as tandem solar cells or solar cells that are optimized for specific regions of the solar spectrum. [72].

4. Lightweight and flexible: PSCs can be made on flexible substrates, such as plastics, which make them lightweight and flexible. This allows for new applications, such as flexible solar panels that can be integrated into clothing or other wearable devices [73].

5. High theoretical efficiency: Theoretical calculations suggest that perovskite solar cells could achieve even higher efficiencies than those currently achieved in the lab. This means that perovskite solar cells have the potential to become even more efficient in the future [74].

2.5 Perovskite for tandem architectures

2.5.1 Silicon solar cell: best candidate for perovskite tandem design

Perovskite tandem solar cells are a type of solar cell that combines two different types of solar cells, one with a high bandgap material and one with a low bandgap material, to capture a broader range of the solar spectrum and increase the overall efficiency of the device. Silicon has been proposed as a bottom cell material in perovskite tandem solar cells due to its well-established manufacturing processes and high efficiency. Additionally, silicon has a bandgap of 1.1 eV, which is very close to the ideal bandgap for a bottom cell in a tandem solar cell. Here are some of the advantages of using silicon as a bottom cell:

1. High efficiency: Silicon solar cells have reached high (PCE) of up to 26.7% in lab conditions. When employed as a bottom cell in a perovskite tandem solar cell, silicon can increase the overall efficiency of the device by capturing the longer wavelength photons that are not absorbed by the perovskite top cell [70].

2. Low cost: Silicon solar cells are a low-cost and well-established technology with a mature manufacturing process. This makes them an attractive option for use as a bottom cell in perovskite tandem solar cells, as the perovskite top cell can be deposited on top of the existing silicon bottom cell.

3. Stability: Silicon solar cells have a high stability and can maintain their performance for decades. This is due to the high stability of silicon as a material and the well-established manufacturing processes used to produce silicon solar cells. This stability is important for perovskite tandem solar cells, as the perovskite top cell can degrade over time.

4. Scalability: Silicon solar cells can be easily scaled up to large areas, which is important for commercial production of perovskite tandem solar cells. Additionally, the well-established manufacturing processes for silicon solar cells can be leveraged for the production of perovskite tandem solar cells.

Overall, using silicon as a bottom cell in perovskite tandem solar cells offers several advantages, including high efficiency, low cost, stability, and scalability. These advantages make silicon an attractive option for use in PVK tandem solar cells and could lead to the development of highly efficient and commercially viable solar energy technology.

2.5.2 SHJ silicon heterojunction solar cell description

Silicon heterojunction solar cells, also known as SHJ solar cells, are a specific type of solar cell that utilizes a combination of crystalline silicon (c-Si) and amorphous silicon (a-Si) layers. The SHJ structure typically consists of a thin layer of amorphous silicon (a-Si) deposited on top of a crystalline silicon (c-Si) wafer. The a-Si layer acts as both the window layer and the emitter, while the c-Si wafer acts as the absorber.

One of the advantages of silicon heterojunction solar cells is their high open-circuit voltage (Voc). The a-Si layer enables the formation of a high-quality junction with the c-Si wafer, resulting in a low interface recombination velocity and a low surface recombination velocity. This allows the solar cell to achieve high Voc values, which is beneficial for overall efficiency.
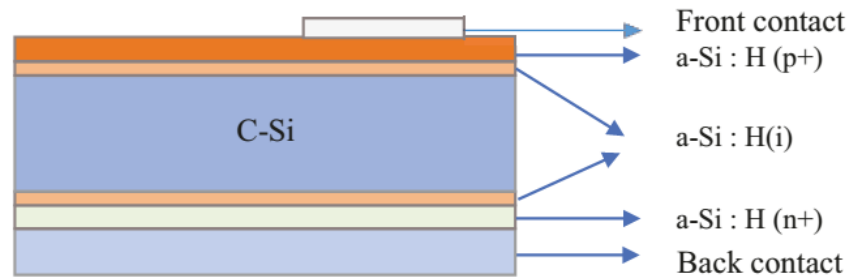
Figure 2.7 SHJ solar cell [75].

The efficiency of the SHJ solar cell improves year after year, rising from 23.7% in 2011 [76] to 24.7% in 2013 with a standard configuration [77], 25.6% in 2014 [76], and 26.3% in March 2017 [77]. Following that, an efficiency of 26.6% was achieved and validated by NREL in 2018 [78]. Today, the finest SHJ solar cell has an efficiency of 26.7% [79]. Figure 2.8 depicts the development of the efficiency of the best SHJ solar cells from 2009 to 2020.
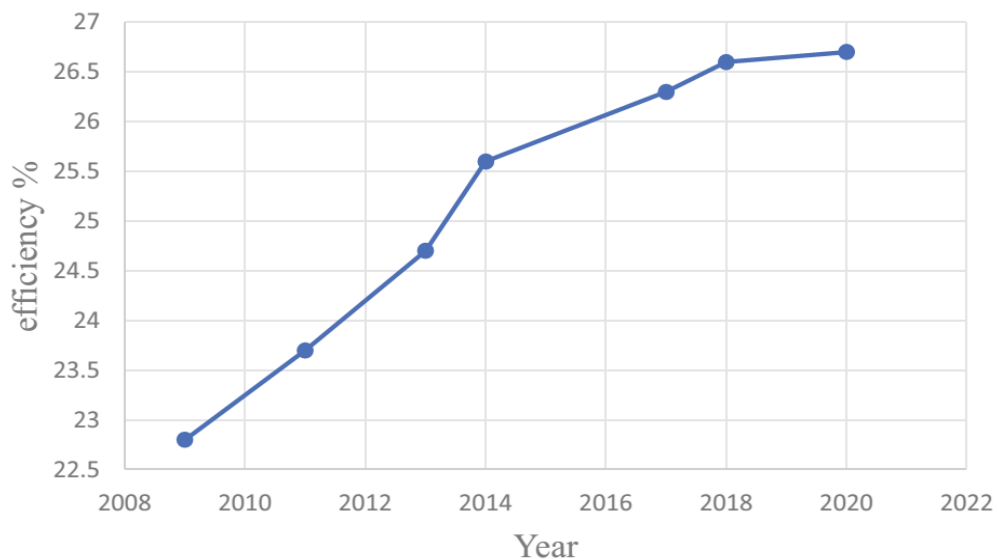
Figure 2.8 SHJ solar cell efficiency evolutions [75].

2.5.3. PVK/Si tandem solar cells

Perovskite on silicon tandem devices are a promising solution to improve the efficiency of photovoltaic beyond the limitations of silicon single junctions. They are easier and cheaper to produce, which has led to a strong interest among scientists. Figure 2.9 illustrates the schematic structure of perovskite-silicon tandem solar cell, where it contains PVK top cell, silicon bottom cell and an interconnection layer between the two layers (top and bottom).
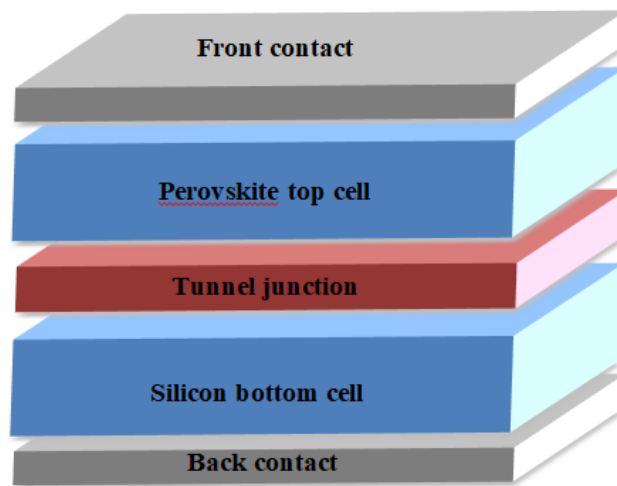
Figure 2.9: Schematic structure of PVK/Si tandem solar cell.

In a recent study by Loper et al. (reference [80]) have focused on perovskite-based organic-inorganic tandems, including a four-terminal tandem solar cell. This cell achieved an efficiency of 13.4% (top cell: 6.2%, bottom cell: 7.2%) and was used to investigate optical losses and derive guidelines for improving efficiency further.

Another study is given by [81] achieved a semi-transparent device by using a transparent silver nanowire electrode on perovskite solar cells, It was used in combination with copper indium gallium diselenide (CIGS) and low-quality multicrystalline silicon to produce solid-state polycrystalline tandem solar cells with a net efficiency gain. This study lights the research for integrating perovskites into a low-cost and high-efficiency (>25%) tandem cell.

In 2021, researchers from Oxford PV, a UK-based company, achieved a world-record efficiency of 29.52% for a perovskite/silicon tandem solar cell. This was certified by the Fraunhofer Institute for Solar Energy Systems ISE in Germany. The record-breaking tandem cell was made using a perovskite solar cell stacked on top of a silicon heterojunction solar cell.

In 2020, another research group from the Helmholtz-Zentrum Berlin für Materialien und Energie (HZB) and the University of Potsdam in Germany achieved an efficiency of 25.2% for a perovskite/silicon tandem solar cell. This was achieved using triple-junction architecture, with two layers of perovskite solar cells stacked on top of a silicon bottom cell.

By the Fraunhofer Institute for Solar Energy Systems (ISE) in Germany (2020), researchers from Helmholtz-Zentrum Berlin and Oxford PV set a new world record for the efficiency of a perovskite silicon tandem solar cell. The device achieved a certified efficiency of 29.1% by optimizing the design of the perovskite layer and improving the interface between the two cells. They also used a new transparent contact material, which allowed more light to enter the cell.

In reference [82], Filipic and his research team examine and deliberate upon the optical characteristics of different tandem designs, including mechanically stacked (four-terminal) and monolithically integrated (two-terminal) tandem configurations. These tandems consist of a methylammonium lead triiodide PSC and a c-Si solar cell as top and bottom cells, respectively. Based on their characterisation, simulations indicate that the four-terminal design can achieve efficiencies of more than 30% with optimised layer thicknesses. It is also possible to reach efficiencies greater than 30% with suitable layer thickness selection and two-terminal monolithic integration of the sub-cells.

Otherwise, Schneider et al. [83] describe an achievable tandem cell structure for light trapping by combining standard pyramidal surface texturing on the Si bottom cell with a wavelength-selective intermediate reflector. This design meets all three optical requirements for high-performance perovskite-on-silicon tandem solar cells: low front surface reflectance, short wavelength light trapping, and strong long wavelength light transmission to the bottom cell. This performance corresponds to 2% to 4% absolute efficiency gains over a planar tandem cell with a single layer ARC on the front surface. They proved that an ideal high-band gap perovskite top cell may attain efficiencies of up to 35% using a basic tandem cell efficiency model.

The next figure shows NREL best research cell efficiencies until the year 2023.
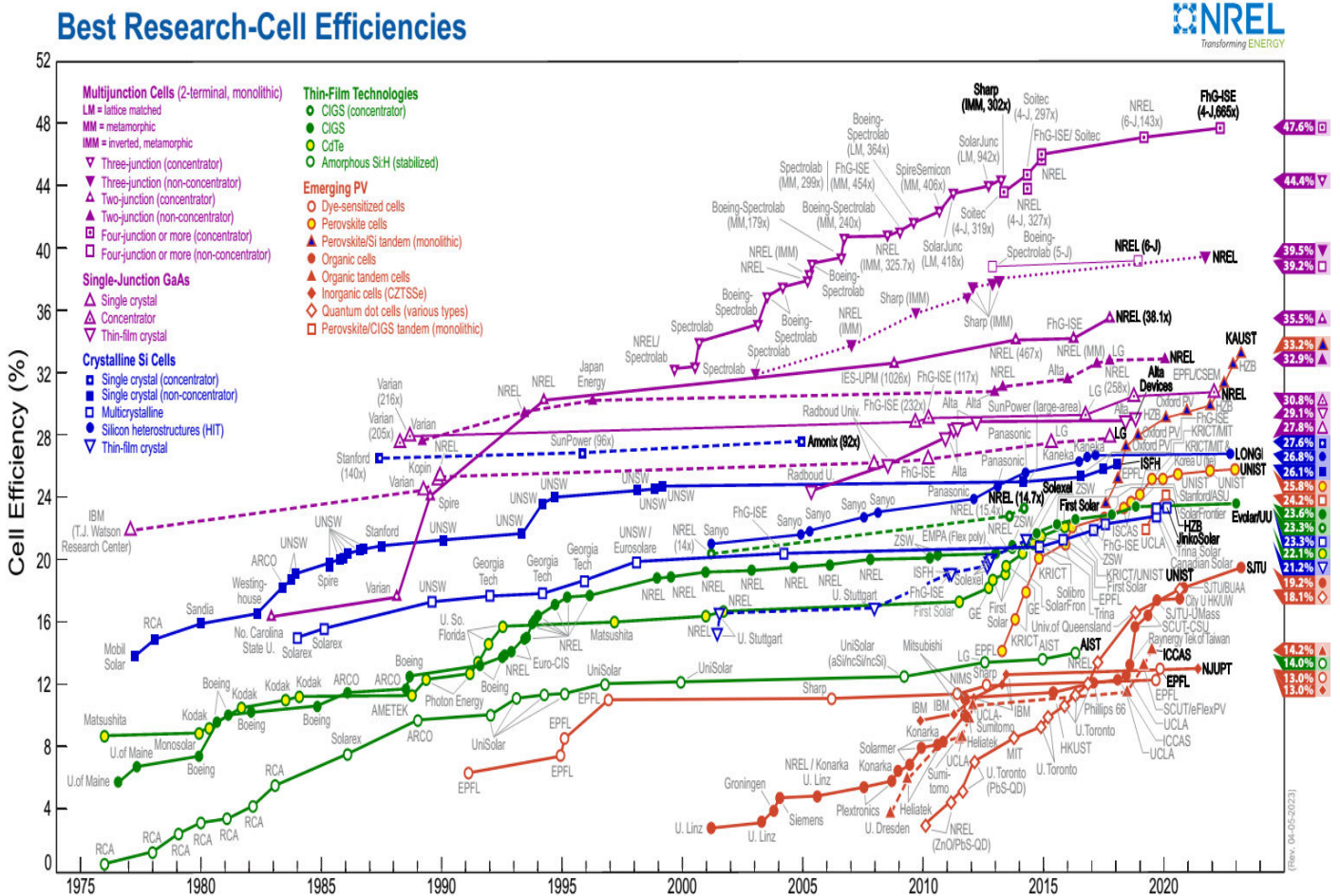
Figure 2.10: Best recorded cell efficiencies reported in NREL including PSCs.

2.6 Efficiency enhancement methods for tandem solar cells

Several characteristics can be explored to better increase the performance of tandem solar cells. The following are the key elements determining their performance:

The use of sub-cells with high efficiency

The efficiency of tandem solar cells can be increased by using sub-cells with record efficiencies and changing the band gaps of bottom cells to lower values and those of top cells to bigger values [84].

Increase the perovskite layer thickness

Current losses can be decreased by increasing the thickness of the perovskite layer, thereby enhancing the efficiency of tandem solar cells [85].

Current-Matching

Optimize the current matching between sub cells to prevent power losses. Adjusting the thickness and doping concentration of each sub cell can help achieve better current matching and minimize losses due to current mismatch.

35

The use of bottom solar cell structure

Choosing the better structure and suitable candidate for bottom cell of the tandem structure may effectively improve the tandem performance more.

Transparent Conductive Layers (TCOs)

Implement transparent conductive layers between sub cells to enhance light transmission and minimize reflection losses. These layers can improve the overall optical properties of the tandem cell, maximizing light absorption.

Optical Design

Utilize advanced optical design techniques, such as anti-reflection coatings and textured surfaces, to reduce reflection losses and increase light trapping within the tandem cell. This improves light absorption and overall efficiency.

4.4 Conclusion

Perovskite/silicon tandem solar cells have emerged as a promising technology in the field of photovoltaic, combining the advantages of both perovskite and silicon solar cells. At the beginning of this chapter, we clarify the key development of multijunction solar cells that have advanced the single junction solar cell issues and limitation which is known as Shockley-Queisser limit. We also discussed the evolution of solar cells: first generation, second generation and third generation. Where in this chapter we focussed on perovskite and perovskite/silicon tandem cells belonging to 3rd generation. In the next two chapters we will investigate the simulated the used structures and give detailed interpretation and discussion of the obtained results.

Chapter 3
Simulation Software

3.1 Introduction

Using simulation modeling can solve currently real-world problems safely and very effectively in a short period of time. It provides an important method of analysis which is easily verified, communicated, and understood. Across industries, simulation modeling provides valuable solutions by giving clear insights into hard and complicated systems.

In order to simulate semiconductor devices particularly designing and modeling solar cells, we have chosen Silvaco simulator to simulate, compare, extract and validate the results of the used structure.

SILVACO (Silicon Valley Corporation) is an American company, located in Santa Clara, California. It is one of the main suppliers of professional chains of finite element simulation and computer-aided design software for electronic technologies TCAD (Technology Computer Aided Design). These tools are used by microelectronics companies in the field of research, development and design of devices.

This chapter presents Silvaco software fundamentals and a review of the atlas command groups and statements and also presents some of the used statements of the simulated structures in our atlas code.

3.2 Overview on Silvaco Atlas simulator

Atlas is a physically-based two and three dimensional system simulator. It predicts the electrical conduct of certain semiconductor constructions and gives perception into the internal physical mechanisms related to machine operation.

Figure 4-1 shows the in and out data of Atlas device, where the most used Atlas simulations input files are Command Files and Structure Files. The 1st input file is a text file that includes instructions for Atlas to execute, while the 2nd input file it describes the structure that will be simulated.

As presented in figure 4-1, DevEdit (Structure and Mesh Editor) and ATHENA (Process Simulator) are used to generate the Structure Files, whereas for DeckBuild (Run Time Environement) it is used to generate the command Files. For the outputs, ATLAS produces three types of output. *Runtime output* provides a guide to the progress of running simulations, where error warning messages appear. *Log-files* store all terminal voltages and currents of the device analysis, and *Solution files* store two- and three-dimensional data related to the value of solution variables inside the device for a single bias point. The two last output files can be exploited by the visualization tool TonyPlot.
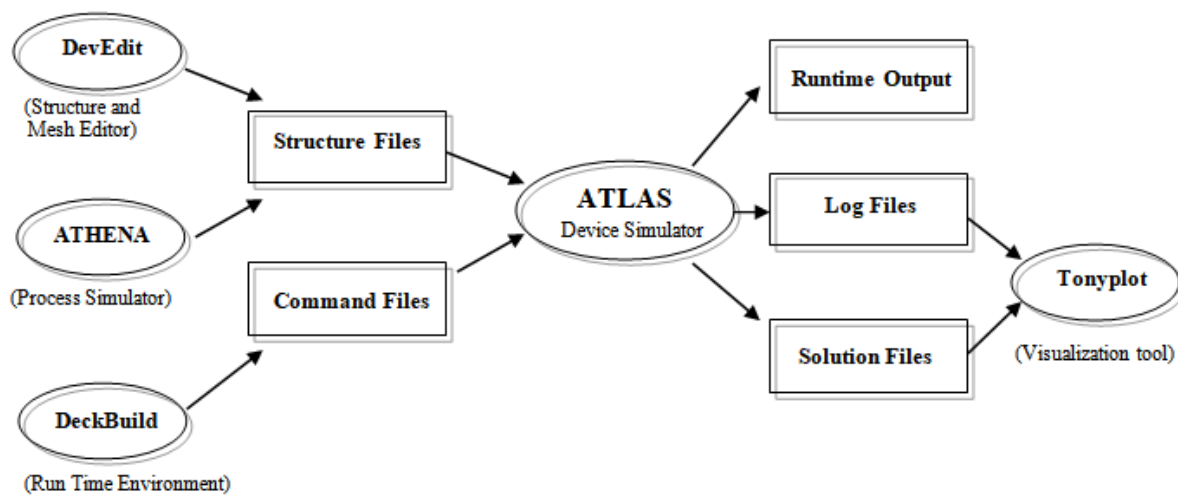
Figure 3.1: Atlas Silvaco inputs and outputs**.**

3.3 Atlas command groups and statements

Atlas commands are divided into five important groups, where these five groups of statements must be classified and executed as presented in figure 4-1.

The order of the ATLAS commands starts with *Structure Specification* which contains (MESH, REGION, ELECTRODE and DOPING), after that the *specification of material models* followed by the *selection of numerical method*. And to end the structure, (LOG, SOLVE, LOAD and SAVE) are the 4 statements to accomplish the *Solution Specification*, while (EXTRACT and TONYPLOT) are the two main statements to present and analyze the *Results*.

Figure 3.2: Atlas command group statements.

3.3.1 Structure Specification

The first step in building a device after the go atlas statement is to define the **MESH**. The mesh is a grid that covers the physical area in which the device is built and simulated. The mesh is simply achieved by a series of user-defined horizontal and vertical lines with spacing between them. Where it can be written in the form bellow:

X.MESH LOCATION=<VALUE> SPACING=<VALUE>

Y.MESH LOCATION=<VALUE> SPACING=<VALUE>

These two statements LACATION and SPACING specify the location of the line and the spacing in microns.

An example of MESH created in ATLAS of our Perovskite structure

#X-Mesh

x.mesh loc=0   spac=0.1

x.mesh loc=1   spac=0.1

#Y-Mesh

y.mesh loc=0   spac=0.002

y.mesh loc=0.01   spac=0.002

y.mesh loc=0.11   spac=0.02

y.mesh loc=0.51   spac=0.02

y.mesh loc=0.61   spac=0.01

y.mesh loc=0.62   spac=0.01

After defining the MESH, the next statement is **REGION**, where the mesh is typically divided into regions. Each region is made of a certain material, which has some default parameters that can be changed or modified. Statements for the regions must be similar to those used for the mesh states to avoid device errors. The region boundary is the most important element of the region statement, where the maximum and minimum x and y are the state's boundaries in the 2D grid.

An example of REGION created in Atlas of our Perovskite structure

#Regions

region num=1   material=ITO   x.min=0 x.max=1   y.min=0   y.max=0.01   conductor

region num=2   user.material=TIO2   x.min=0   x.max=1   y.min=0.01   y.max=0.11/ donor=1e16

region num=3   user.material=perovskite   x.min=0   x.max=1   y.min=0.11   y.max=0.51/ donor=1e16

region num=4   user.material=spiro   x.min=0   x.max=1 y.min=0.51   y.max=0.61/ acceptor=2e18

region num=5   material=Silver   x.min=0   x.max=1   y.min=0.61   y.max=0.62   conductor

The ELECTRODES are the statement that follows the MESH. It can be defined as:

#Electrodes

electrode name=cathode top

electrode name=anode bottom

Usually using this declaration of electrodes by the user is sufficient for solar cell modeling to only cover the top and bottom of the cell structure.

To specify the position of electrodes on the device structure on any specific region, the user must use the next declaration to describe minimum and maximum position boundaries; XMIN, XMAX, YMIN, YMAX.

ELECTRODE NAME = <electrode name> <position>.

The next statement is **DOPING**, it specifies the doping levels regions of the device structure. This statement includes four other statements (doping distribution, region specification, dopant type, and region number) which affect the electrical properties of the structure.

DOPING <distribution type> <dopant type> <position parameters>.

The doping distribution can be Uniform, Gaussian or non-standard distributions to generate the doping profile, while for the dopant type, the region could be *n* doped or *p* doped. Or it can also be declared in the statement REGION as mentioned earlier as *donor* (n type) and *acceptor* (p type).

3.3.2 Material Models Specification

After defining the different statements of Structure Specification, the following statement is **MATERIAL**. The user describes the MATERIAL and its properties using the form bellow:

MATERIAL <localization> <material definition>.

An example of MATERIAL created in ATLAS of our Perovskite/Silicon structure:

#Material Properties

#TiO2

material mat=Tio22 user.group=semiconductor user.default=ZnO TAUN=1.0E-7/ TAUP=1.0E-7 MUN=20 MUP=10 NC300=2.2e18 NV300=1.8e19 EG300=3.20/ AFFINITY=3.9 PERMITTIVITY=9

material mat=Tio22 index.file=tio22.nk

#Spiro

material mat=spiro user.group=semiconductor user.default=GaN TAUN=1.0E-7/ TAUP=1.0E-7 MUN=2e-4 MUP=2e-4 NC300=2.2e18 NV300=1.9e19 EG300=3.00/ AFFINITY=2.45 PERMITTIVITY=3.0

material mat=spiro index.file=spiro.nk

#Perovskite

material   mat=PEROVSKITE   user.group=semiconductor   user.default=GaAs   TAUN=1E-6/
TAUP=1E-6 MUN=2 MUP=2 NC300=2.2e18 NV300=1.8e19 EG300=1.585/
AFFINITY=3.9   PERMITTIVITY=6.5

material mat= PEROVSKITE   index.file= PEROVSKITE.nk

#n-aSi

material   region=6   taun0=1e-6   taup0=1e-6   eg300=1.72   nv300=2.5e20   nc300=2.5e20/
PERMITTIVITY=11.9 AFFINITY=3.8

mobility region=6 mun=10 mup=2

material region=6 index.file=n-aSi.nk

#i-aSi

material   region=7   taun0=1e-6   taup0=1e-6   eg300=1.72   nv300=2.5e20   nc300=2.5e20/
PERMITTIVITY=11.9 AFFINITY=3.8

material region=7 index.file=i-aSi.nk

mobility region=7 mun=20 mup=5

#c-Si

material   region=8   taun0=1e-3   taup0=1e-3   eg300=1.12   nc300=2.8e19   nv300=1.04e19/
PERMITTIVITY=11.9 AFFINITY=4.05

mobility region=8 mun0=1350 mup0=450

material region=8 index.file=c-Si.nk

#i-aSi

material   region=9   taun0=1e-6   taup0=1e-6   eg300=1.72   nv300=2.5e20   nc300=2.5e20/
PERMITTIVITY=11.9 AFFINITY=3.8

mobility region=9 mun=20 mup=5

material region=9 index.file=i-aSi.nk

#p-aSi

material   region=10   taun0=1e-6   taup0=1e-6   eg300=1.72   nv300=2.5e20   nc300=2.5e20/
PERMITTIVITY=11.9 AFFINITY=3.8

mobility region=10 mun=10 mup=2

material region=10 index.file=p-aSi.nk

The optical properties of several used materials are listed in the Sopra database of the ATLAS program. The user can generate and create an input file (.nk .n or .k file) to set the optical characteristics of a material even if it isn't in the Sopra database.

MODELS statement is the next to be investigated. A designer can select from more than 70 models in ATLAS to utilize in order to increase the precision and accuracy of the simulated structure.

An example of MODELS statement of our tandem structure

models srh print temp=300

Table 3-1:Models notes used during the simulation

Parameter	Syntax	Notes
Shockley-Read-Hall	SRH	Recombination model that uses fixed minority carrier lifetimes. Most simulations utilize SRH recombination
Operating Temperature	TEMPERATURE	A parameter defining the operating temperature
Model and Parameter Verification	PRINT	a parameter that, in the run-time output, lists the simulation's models and parameters, enabling verification of their accuracy

And for the **CONTACTS**. The contact determines and describes the assignments of the electrodes. The contact syntax is:

CONTACT NAME=<name> <property_specification>

An example of CONTACTS statement:

Contact name=anode   workf=4.9

Contact name=cathode workf=4.5

If the properties of the electrodes do not require any specific modification or designation, the CONTACT declarations are not necessary [86].

At interfaces between semiconductors and insulators, the **INTERFACE** statement is used to indicate the interface charge density and surface recombination velocity [86]. The format of the INTERFACE statement is as follows.

INTERFACE <parameters> <interface_dimensions>

An example of INTERFACE statement:

Interface x.min=0 x.max=5 y.min=0 y.max=0 s.n=1e-7 s.p=1e7

In this thesis, interface properties are not utilized in our simulated solar cells.

3.3.3 Numerical Specification

METHOD is the only statement in the Numerical Specification. The behavior of semiconductor devices can be calculated and determined using a variety of method types. Three fundamental categories of strategies exist among these methods for obtaining the solutions: decoupled (GUMMEL), fully coupled (NEWTON), and decoupled and fully coupled (BLOCK). The general format for the METHOD statement is as follows.

METHOD <methods>

An example of METHOD statement used in our tandem structure

method newton

Newton METHOD is the used default method in Atlas simulator and it is the most preferred used to solve

3.3.4 Solution Specification

LOG saves all the final simulation characteristics in a data file. Any type of data generated by the Solve command is saved after the LOG command. If there are several LOG commands in the program, each time the log file that was opened before is closed and a new log file is opened [87]

SOLVE instruction follows the LOG instruction it performs a solution for one or more bias points.

The **LOAD** and **SAVE** statements are used together to help create better initial guesses for bias points. The SAVE statement saves simulation results into files for visualization or for future use as an initial guess, and after that the LOAD statement loads a solution file whenever required to assist in the solution.

3.3.5 Results Analysis

The results analysis consists of **EXTRACT** and **TONYPLOT** statements that describe how to treat the solutions determined in the ATLAS simulation.The EXTRACT statement is provided within the DeckBuild environment. It has a flexible syntax that allows the user to extract device parameters and construct specific EXTRACT 52 routines. [56]

All graphics in ATLAS^{TM} are created by saving and loading the file into TONYPLOT command. The log files and the current-voltage cell characteristic can be plotted and observed in TONYPLOT. [56]

An example of EXTRACT and TONYPLOT created in ATLAS of our tandem structure:

Extract name="IV" curve(v."anode", i."cathode")

#Plot

Extract init infile="tandem_cell.log"

Extract name="Isc" max(i."cathode")

Extract name="JscmAcm2" $Isc*1e03

Extract name="Voc" x.val from curve(v."anode", i."cathode") where y.val=0.0

Extract name="Pm" max(curve(v."anode", (v."anode" * i."cathode")))

Extract name="P" curve(v."anode", (v."anode" * i."cathode")) outf="tandem_cell_power.dat"

Extract name="iv" curve(v."anode", i."cathode") outfile="tandem_cell.dat"

Extract name="Vm" x.val from curve(v."anode", (v."anode"*i."cathode")) where y.val=$"Pm"

Extract name="Im" $"Pm"/$"Vm"

Extract name="FF" ($"Pm"/($"Isc"*$"Voc"))*100

Extract name="Opt_int" max(beam."1")

Extract name="Eff" ($Pm/($"Opt_int"))*100

Tonyplot tandem_cell.dat

Figures 3.3, 3.4, 3.5 and 3.6 present perovskite, SHJ and tandem cells for perovskite structure and IV curves using TONYPLOT statement
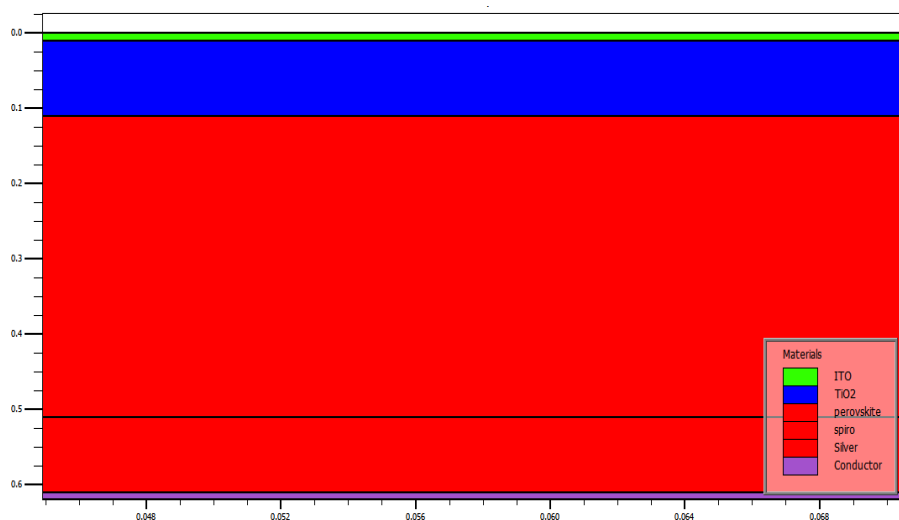
Figure 3.3: Perovskite structure using Tonyplot statement.
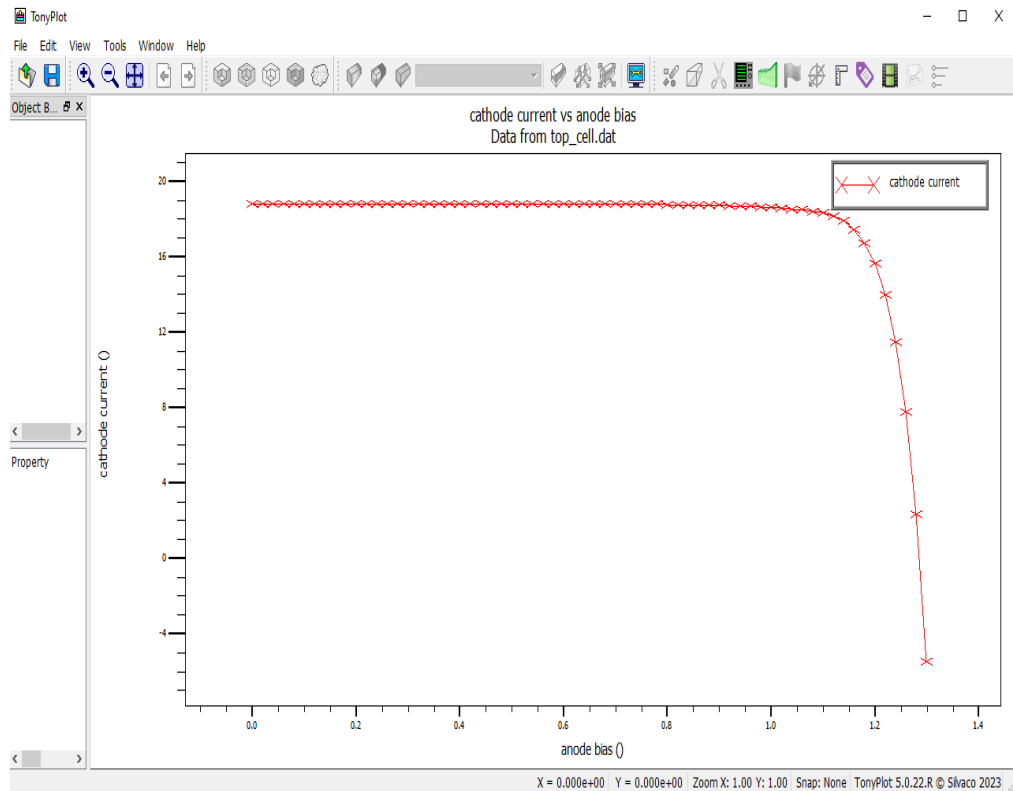
Figure 3.4: IV curve for perovskite top using Tonyplot statement.
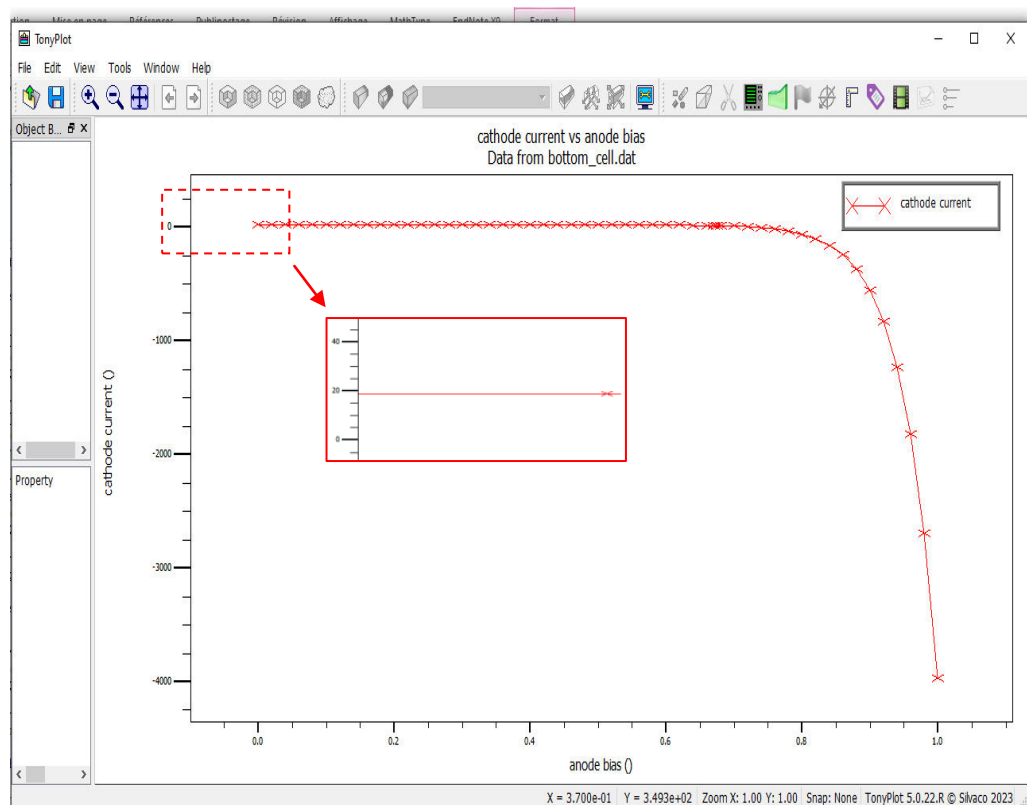
Figure 3.5: IV curve for cell SHJ bottom cell using Tonyplot statement.
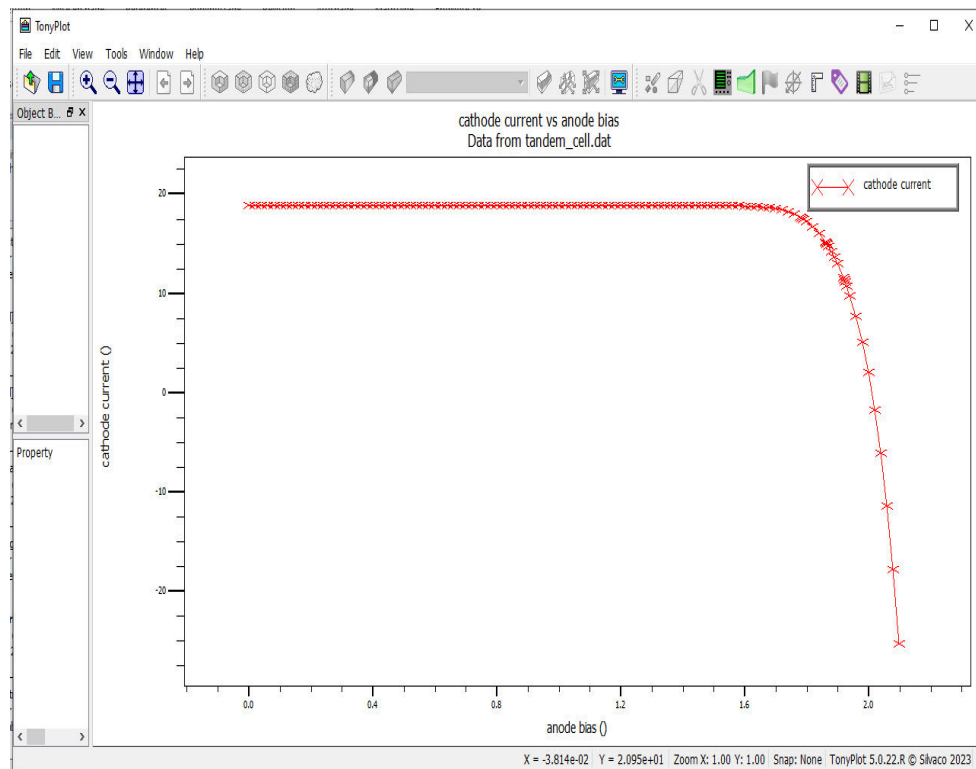
Figure 3.6: IV curve for tandem cell using Tonyplot statement.

3.4 Conclusion

In this section, we have introduced an overview on Silvaco simulator and we have also presented Atlas command groups and statements in details. The cell structure is defined using Deckbuild code, setting the structure mesh, regions, electrodes, doping levels, and material properties. The ATLAS program then identifies solutions for all solve statements and in accordance with the user's instructions it saves the results in log and structure files. At the end the data file is created and extracted by EXTARCT command, and then the results will be plotting by TONYPLOT command.

Chapter 4

Numerical simulation and optimization of CH3NH3PbI3-xBrx single perovskite and Perovskite/Silicon tandem solar cells

4.1 Introduction

Photovoltaic cells have become one of the solutions for dealing with the challenges of renewable energy supply in our society. Solar cell research is a growing and interesting field that includes silicon solar cells, organic solar cells, dye sensitised solar cells (DSSCs), and perovskite solar cells (PSCs). Among those cells, PSCs are the most emerging area of research among different new generation photovoltaic technologies due to its low cost manufacturing and high power conversion efficiency. Hence, these characteristics make this essential aspect of perovskites particularly appealing for multi-junction or tandem solar cell configurations.

In this chapter, we have designed and investigated Perovskite/Silicon tandem solar cell where our work is divided into two simulation parts, in the **1st part** we have simulated the single CH$_3$NH$_3$PBI$_{3-x}$Br$_x$ perovskite solar cell in order to improve the power conversion efficiency (PCE) of the cell. And in the **2nd part**, we have studied the effect of the top cell perovskite thickness on different output parameters V$_{oc}$, J$_{sc}$, FF and efficiency of PVK/Si tandem device with the aim of achieving the current matching condition between top, bottom and tandem cells.

4.2 Part 1: Modelling of MAPbI$_{3-x}$Br$_x$ based solar cell for high PCE

In this part of simulation, we analyze the behavior of perovskite solar cell (PSC) by improving the different layers thickness of the utilized design. Our modelled architecture incorporates methylammonium mixed bromide-iodide lead perovskite, $CH_3NH_3PbI_{3-x}Br_x$ ($0 \leq x \leq 1$). The used active layer is positioned between layers of TiO_2 and Spiro-OMeTAD. The aim of this initial part is to enhance the efficiency by varying the thicknesses of all the regions.

4.2.1 Simulation method of the modelled structure

4.2.1.1 Device structure

Based on an experimental architecture [88], the simulated structure consists of $TiO_2/CH_3NH_3PbI_{3-x}Br_x$/Spiro-OMeTAD (figure 4.1). In this structure TiO_2 (0.2 µm) acts as electron transport material (ETL), this ETL is recognized for its favorable band alignment, exceptional optoelectronic properties, and stability, [89, 90] and spiro-OMeTAD (0.9 µm) as hole transport layer (HTL), a material largely used for high efficient solar cells. The mixed halide perovskite $CH_3NH_3PbI_{3-x}Br_x$ (0.5 µm) is as n-type absorber layer, whereas the HTL and ETL correspond to p-type and n-type layers, respectively.
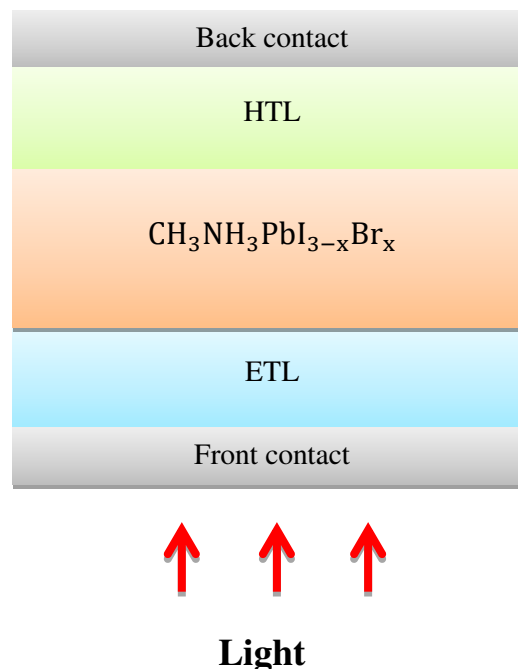
Figure 4.1: Device structure.

The inputs parameters employed for each region within the PSC structure can be found in Table 4.1. The simulation parameters of TiO_2, Spiro-OMeTAD, and PVK layer are adopted from a previously published simulation design in the literature [91]. The absorber and HTL absorption coefficients have been taken from refs [89, 90], whereas for ETL, the absorption coefficients are available in the Silvaco library's SOPRA database. While for the band gap of $CH_3NH_3PbI_{3-x}Br_x$, its equation as a function of x is calculated and deduced from literature [88], Eg=1.565+0.15x. Shockley-Read-Hall (SRH) recombination is the physical model employed in this simulation. In simulations, Newton's iterative approach is used to achieve and ensure convergence for the solution method of Poisson's equation and continuity equations. AM1.5 spectrum illumination is used for photocurrent density-voltage (I-V characteristics).

Table 4.1 The selected parameters for the used material.

Material property	TiO_2	$CH_3NH_3PbI_{3-x}Br_x$	Spiro-OMeTAD
Thickness (nm)	variable	variable	Variable
Band gap (eV)	3.2	variable	3
Affinity (eV)	3.9	3.9	2.45
Permittivity	9	6.5	3
N_C (cm^{-3})	2×10^{18}	2.2×10^{18}	2.2×10^{18}
N_V (cm^{-3})	2×10^{19}	1.9×10^{19}	1.9×10^{19}
N_D (cm^{-3})	0	1×10^{16}	1×10^{16}
N_A (cm^{-3})	2×10^{18}	0	0
μ_n (cm^{2}V^{-1}S^{-1})	0.2	2	2×10^{-4}
μ_p (cm^{2}V^{-1}S^{-1})	0.1	2	2×10^{-4}
τ_n(s)	1×10^{-7}	variable	1×10^{-7}
τ_p(s)	1×10^{-7}	variable	1×10^{-7}

4.2.1.2 Simulation method

The structure TiO_2/$CH_3NH_3PbI_{3-x}Br_x$/Spiro-OMeTAD as illustrated in figure 4.2 has been modelled by changing x-values ($CH_3NH_3PbI_{3-x}Br_x$). Hence, the bandgap vary as a function of x, where x range is between [0-1]. Table 4.2 shows experimental and simulation results with different charge carrier lifetimes (τ) mentioned in literature.

Table 4.2 Measured and simulated outcomes with various x-values

$CH_3NH_3PbI_{3-x}Br_x$			Experiment [87]	Simulation
x-values	Eg (eV)	Taux (ns)	PCE (%)	PCE (%)
x=0	1.565	52	15.60	17.61
x=0.09	1.579	39	16.31	18.24
x=0.11	1.585	35	16.75	19.49
x=0.14	1.591	34	18.02	18.61
x=0.20	1.597	33	17.11	17.41
x=1	1.725	15	3.83	2.93

According to the simulation results, the highest achievable PCE reached 19.49% with specific values of x=0.11, Eg=1.585 eV and $\tau = 3.5 \times 10^{-8}s$. This optimal PCE will be improved using the following three steps to obtain the best thickness for each region that is appropriate to have high PCE. Initially, the HTL and ETL thicknesses were set at 900 and 100 nm, respectively, while the PVK layer thickness was adjusted between 100 and 900 nm. Secondly the optimal thickness for the perovskite layer with the maximum efficiency was determined. The ETL layer thickness was also fixed at 100 nm, while the HTL thickness ranged from 100 nm to 900 nm. Finally, the optimal thickness for the HTL layer was fixed along with the perovskite layer thickness that have been already fixed, while the ETL layer thickness was varied from 100 nm to 900 nm. Subsequently, a comprehensive discussion of the resulting design will be presented in the results section.

4.2.2 Results and discussions

As seen in figure 4.2, the output parameters vary as the PVK layer thickness increases, and this is regarded as a limiting factor for the cell's behaviour. Figure 4.2(a) shows a high open circuit voltage at 0.2 µm, indicating of less recombination, followed by a reduction in V_{oc} against absorber thickness, indicating that the larger thickness generates more carriers and recombination. In figure 4.2(b), it is noticed that J_{sc} rises with absorber layer thickness because photons obtain a longer path for absorption and therefore produce more carriers. The fill factor (FF) and power conversion efficiency are shown in Figures 4.2(c) and 4.2(d), respectively. The obtained results show a significant drop in the FF, which could indicate an increase in series resistance in the cell induced by a rise in absorber thickness. The PCE curve resembles to that of short circuit current density, it grows up to 400 nm as the perovskite thickness was rised with

PCE of 19.84 % because of the absorption of more light. The effect of HTL thickness on V_{oc}, J_{sc}, FF and PCE is not significant in figure 4.3, possibly due to the absorption of most photons accessible in the absorber and ETL layers, and very few carriers created in the HTL layer.

As shown in figure 4.3(a) and figure 4.3(b), the value of V_{oc} and J_{sc} is around 1.13V and 22 mA/cm^2, respectively. Figures 4.3(c) and 3(d) indicate that the FF and PCE are almost stable at around 77% and 20%, respectively. Figure 4.4 show that the thickness of the ETL has no impressive impact on the electrical parameters (Voc, Jsc, FF, and PCE). This is because the number of charge carriers produced in the PVK material is constant.

According to figures 4.2-4.4, the best PCE value for the perovskite layer is 20.35%, and the optimised thicknesses for perovskite, ETL, and HTL are 400 nm, 100 nm, and 100 nm, respectively.
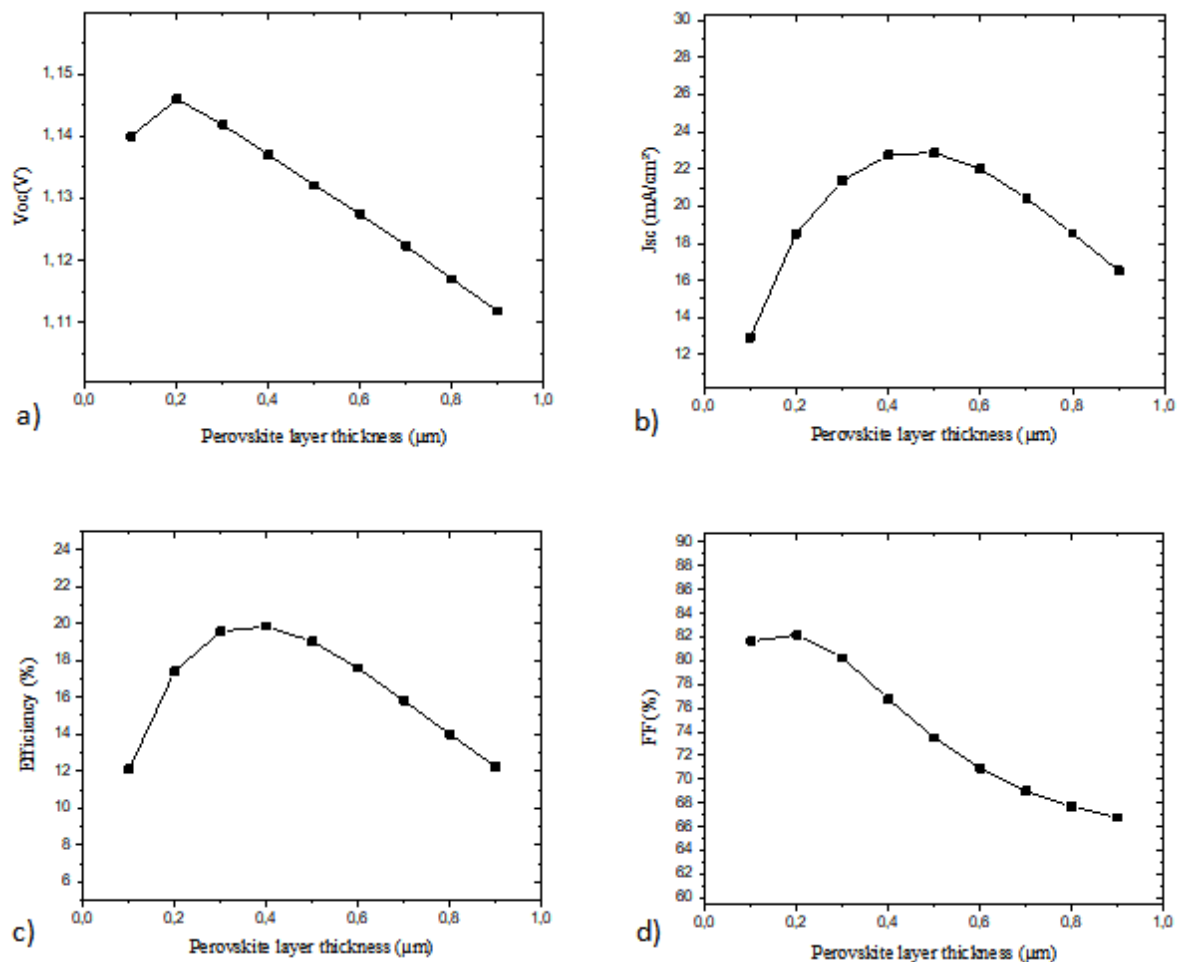
Figure 4.2: Influence of PVK thickness on different output parameters.
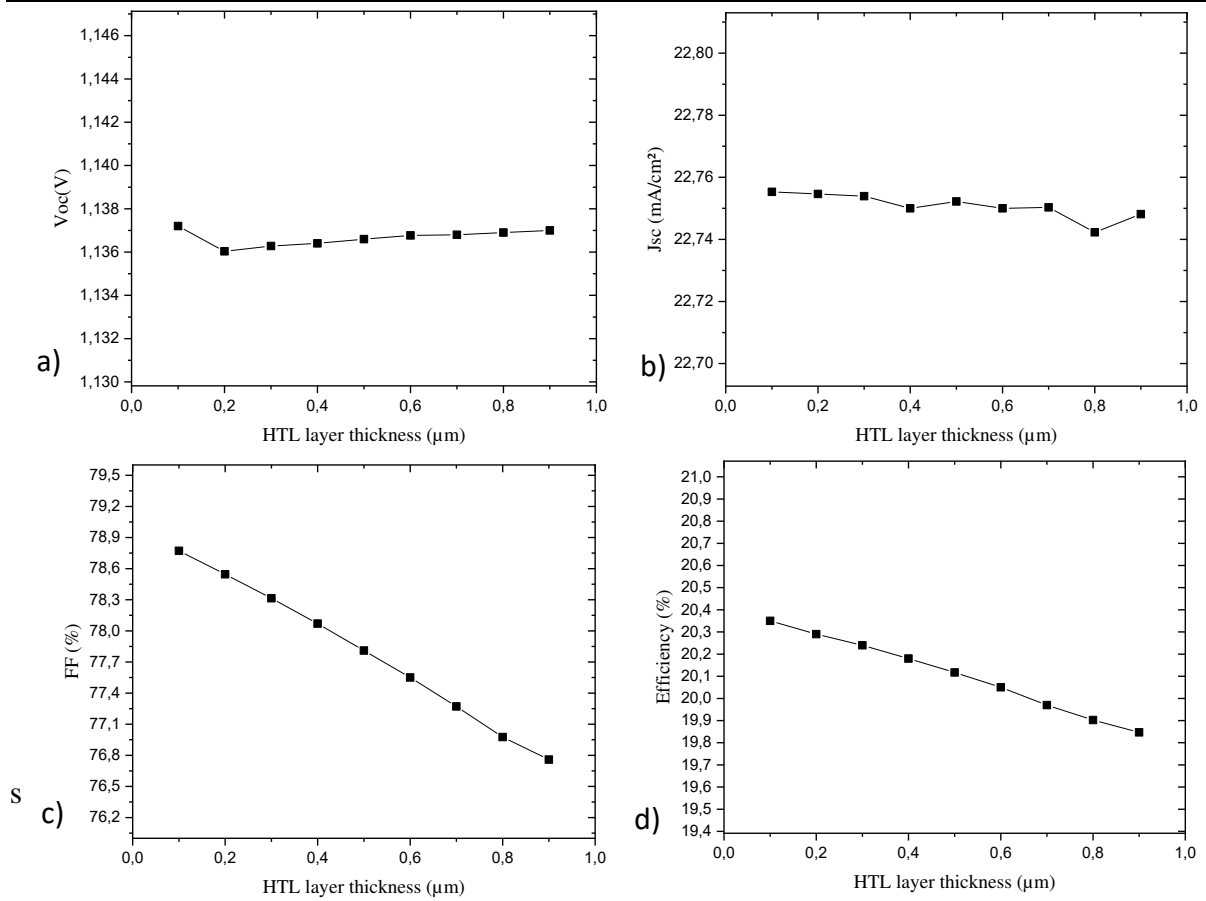
Figure 4.3 Influence of HTL thickness on different output parameters.
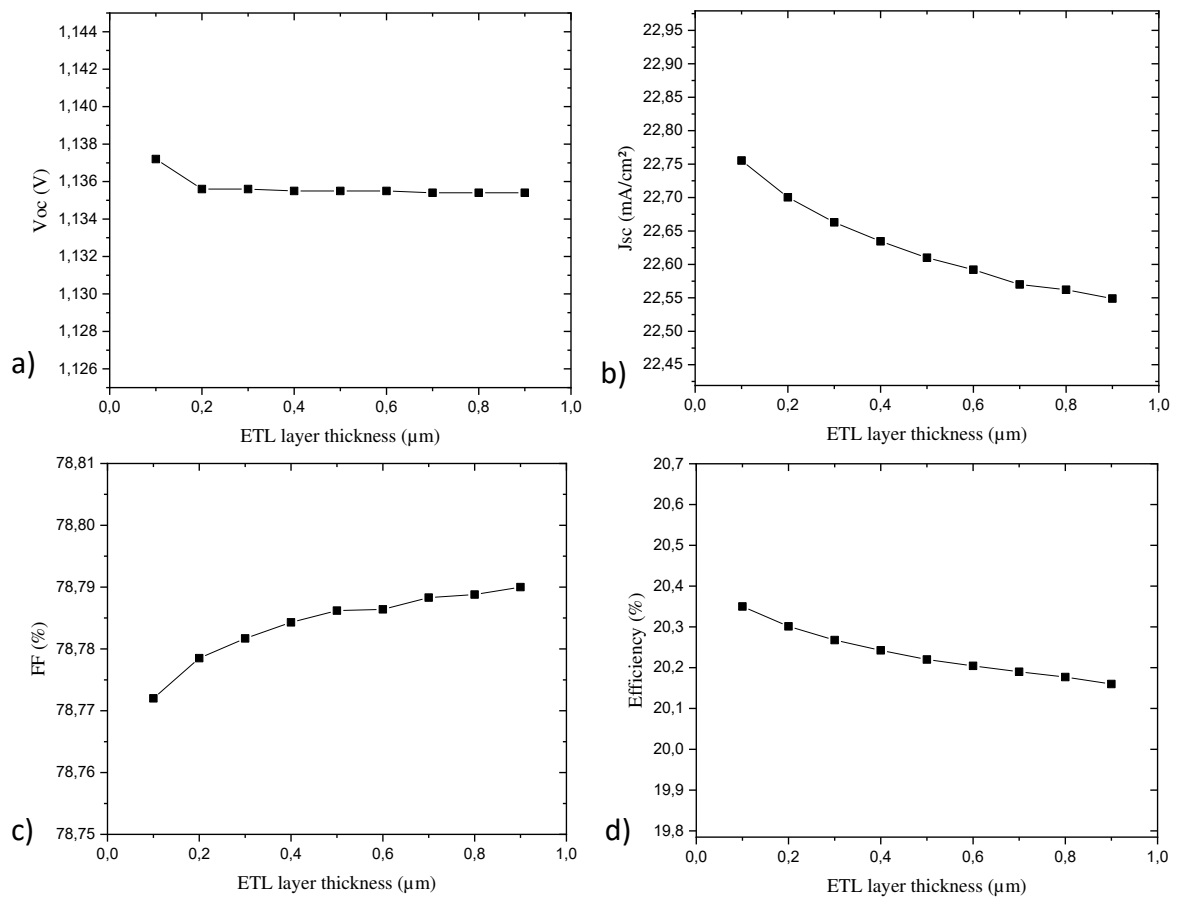
Figure 4.4: Influence of ETL thickness on different output parameters.

55

Table 4.3 compares the derived design structure with optimized layer thicknesses to the no-optimized cell, reference cell [88], and optimized design (with longer carrier lifetime). Figure 4.5 displays the current-voltage curves of the experimental structure and our simulations; from this figure, it is clear that the optimized designs achieve good enhancement compared to no-optimized one. Depending on the obtained results, there is a good match between reference cell [88] and our simulation results.

4.2.2.1 Carrier lifetime optimization

The gained PCE (20.35%) might be improved to 24.72% by adopting a longer carrier lifetime (10^{-6} s) in the PVK material [92]. Table 4.3 outlines the electrical output parameters of simulated and reference [88] devices.

Table 4.3 PV parameters extracted from simulated and measured I-V curves

	V_{oc} (V)	J_{sc} (mA/cm^2)	FF (%)	Efficiency (%)
Reference cell [87]	1.064	23.52	72	18.02
No-optimized cell	1.13	22.90	75.27	19.49
Optimized thickness	1.137	22.75	78.77	20.35
Optimized cell (with longer carrier lifetime)	1.22	23.13	87.16	24.72

Figure 4.5 presents I-V curves of simulated results compared with reference cell.
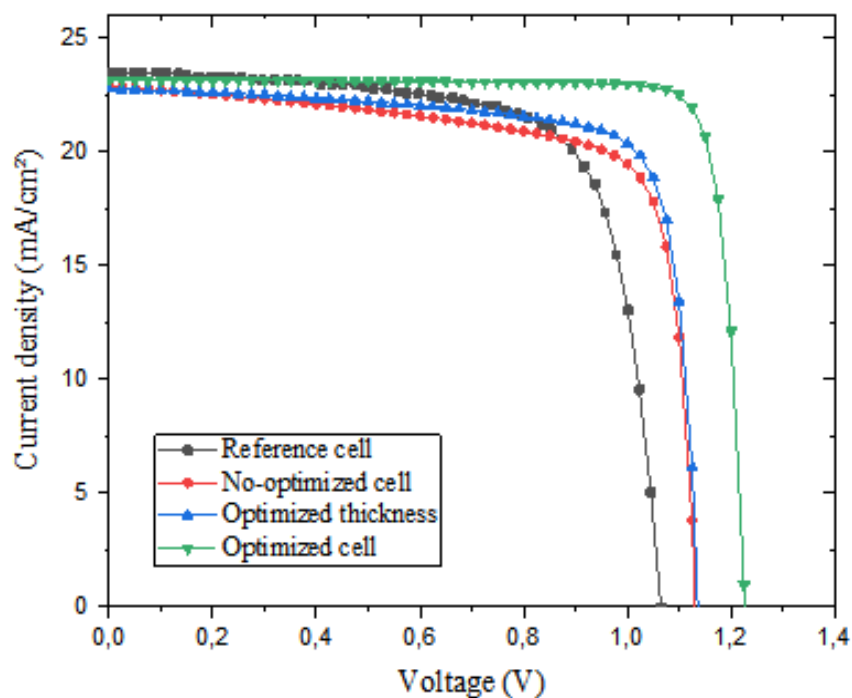
Figure 4.5: I-V curves of the PSCs based on $CH_3NH_3PbI_{3-x}Br_x$.

4.3 Part 2: Influence of PVK thickness on the performance of PVK/Si tandem solar cell

This part investigates the simulation of a PVK/SHJ tandem solar cell, based on $CH_3NH_3PbI_{3-x}Br_x$ and Silicon-hetero-junction (SHJ) as top and bottom cells, respectively. Firstly, we have simulated the single perovskite and the single silicon solar cells. Secondly, we have modeled the Perovskite/Silicon tandem solar cell showing a mismatched current between the sub-cells. Finally, by studying the effect of the top cell thickness on the tandem device we achieved the current matching condition between the cells reaching high conversion efficiency.

4.3.1 Tandem structure and simulation parameters

4.3.1.1 PVK/Si solar cell design

In this work, we utilized Silvaco ATLAS software to design a tandem solar cell. This software is counting on mathematical models that incorporate Poisson's equation, continuity equations, and transport equations. Our design, as depicted in Figure 4.6, comprises a top cell consisting of Perovskite ($CH_3NH_3PbI_{3-x}Br_x$) [93] and a bottom cell made of Silicon Hetero-junction (SHJ). To ensure optimal operation of the tandem solar cell, it is essential for the energy band gap of the top cell to be greater than that of the bottom cell. Consequently, Eg of $CH_3NH_3PbI_{3-x}Br_x$ is set at 1.585 eV with x=0.11 and Eg of Silicon (1.12 eV). The tandem solar cell's detailed design includes an n-TiO_2, n-Perovskite and p-Spiro-OMeTAD, where TiO_2 and Spiro-OMeTAD are electron and hole transport layers (ETL) and (HTL), respectively Regarding the Silicon Hetero-junction (SHJ) solar cell, we conducted simulations and compared the results with references [94- 96], which consists of n-a-Si (10nm), i-a-Si (5nm), n-c-Si (300µm), i-a-Si (5nm), p-a-Si (10nm). To connect the two sub-cells, we employed an interconnection layer of ITO (10 nm), which is the most commonly used transparent conductive oxide (TCO) material since it is both optically transparent and electrically conductive.

Light
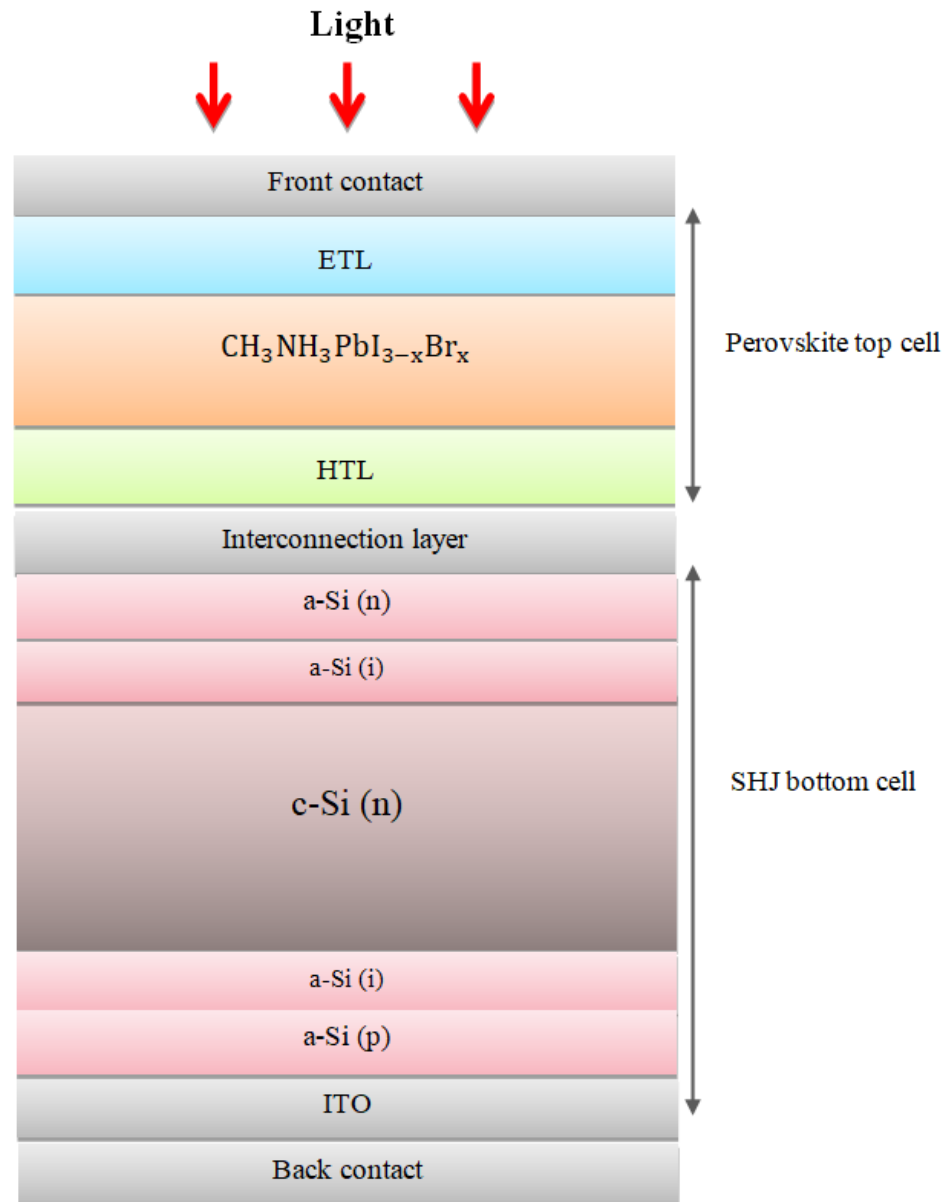
Figure 4.6: Device structure.

4.3.1.2 Simulation parameters

The employed tandem structure in this work consists of $TiO_2 / CH_3NH_3PbI_{3-x}Br_x$ /Spiro-OMeTAD as a perovskite top cell [93]. The bottom cell comprises n-a-Si/i-a-Si/n-c-Si/i-a-Si/p-a-Si, as described in literatures [19, 97]. These two sub-cells are interconnected using the transparent conducting oxide ITO. A comprehensive list of all simulated parameters used in this study is presented in Table 4.4. Top and bottom cells input parameters are given in references [93, 96] and [19], respectively. The absorption coefficients of the materials employed (HTL, perovskite, a-Si, and c-Si) were obtained from the references [97-99, 18], whilst the ETL material was obtained from the Silvaco library. To address convergence

problems, the iterative methods of Newton and maxtrap were used. The numerical simulations employed the SRH model to describe the recombination process. Lastly, the simulations were conducted under AM1.5G spectrum illumination.

Table 4.4 Device parameters of the used materials.

Material property	TiO$_2$	CH$_3$NH$_3$PbI$_{3-x}$ Br$_x$	Spiro-OMeTAD	a-Si(i)	a-Si(n)	a-Si(p)	c-Si
Thickness (µm)	0.05	0.280	0.05	0.005	0.01	0.01	300
Eg (eV)	3.2	1.585	3	1.72	1.72	1.72	1.12
Affinity (eV)	3.9	3.9	2.45	3.8	3.8	3.8	4.05
Permittivity	9	6.5	3	11.9	11.9	11.9	11.9
N$_C$ (cm^{-3})	2×10^{18}	2.2×10^{18}	2.2×10^{18}	2.5×10^{20}	2.5×10^{20}	2.5×10^{20}	2.8×10^{19}
N$_V$ (cm^{-3})	2×10^{19}	1.9×10^{19}	1.9×10^{19}	2.5×10^{20}	2.5×10^{20}	2.5×10^{20}	1.04×10^{19}
N$_D$ (cm^{-3})	1×10^{16}	1×10^{16}	0	0	1×10^{19}	0	3×10^{15}
N$_A$ (cm^{-3})	0	0	2×10^{19}	0	0	6×10^{18}	0
µ$_n$ (cm²V^{-1}S^{-1})	0.2	2	2×10^{-4}	20	10	10	1350
µ$_p$ (cm²V^{-1}S^{-1})	0.1	2	2×10^{-4}	5	2	2	450
τ$_n$(s)	1×10^{-7}	1×10^{-6}	1×10^{-7}	1×10^{-6}	1×10^{-6}	1×10^{-6}	1×10^{-3}
τ$_p$(s)	1×10^{-7}	1×10^{-6}	1×10^{-7}	1×10^{-6}	1×10^{-6}	1×10^{-6}	1×10^{-3}

4.3.2 Results and discussion

4.3.2.1 Modelling of the single PVK and SHJ solar cells

The structural configuration of the perovskite CH$_3$NH$_3$PbI$_{3-x}$Br$_x$ s illustrated in Figure 4.7. It consists of titanium dioxide TiO$_2$ as ETL, Spiro-OMeTAD as HTL and an n-type perovskite absorber material. In our simulation, we used a schematic structure with a bromide (Br) ratio of x=0.11 for the CH$_3$NH$_3$PbI$_{3-x}$Br$_x$. This structure was simulated with various x-values in the first part and compared to experimental results [88]. The optimal efficiency was obtained with x=0.11 and E$_g$=1.585 eV. The doping concentrations for the perovskite cell are specified in Table 4.4, while the thicknesses of each layer are set at 50 nm for ETL, 50 nm for HTL, and 280 nm for the perovskite layer.
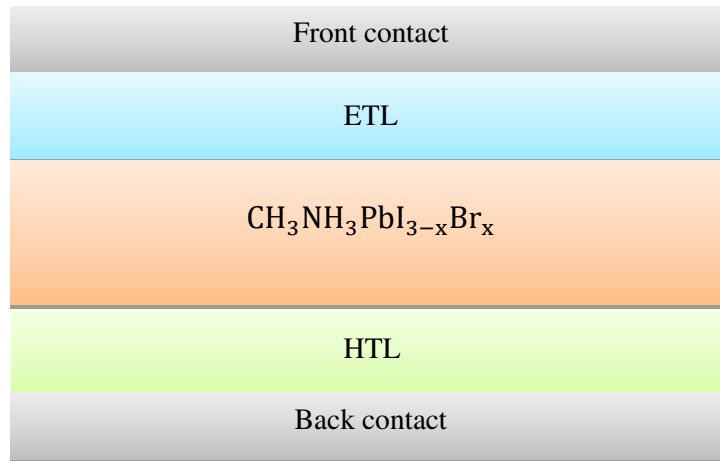
Figure 4.7: Single perovskite top cell structure.

The design of the SHJ structure is adopted in the next refs [18, 19]. This cell configuration includes front contact ITO, followed by layers of n-a-Si (10 nm), i-a-Si (5 nm), n-c-Si (300 µm), i-a-Si (5 nm), p-a-Si (10 nm), ITO (150 nm), and finally, a back contact made of Ag. Figure 4.8 presents the layers in the SHJ structure, with the crystalline silicon Eg =1.12 eV.
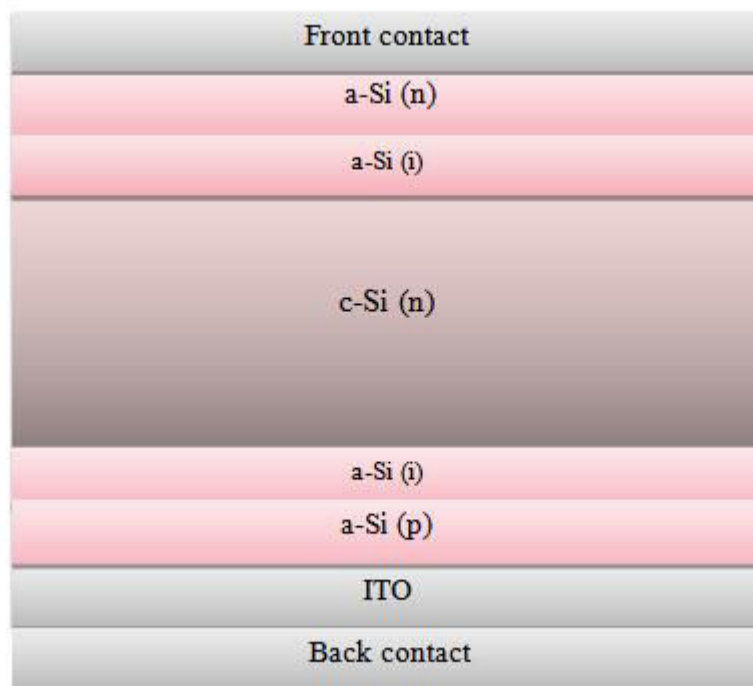
Figure 4.8: Single Silicon Hetero-junction bottom cell structure.

Figure 4.9 depicts the I-V curves of single top and bottom sub-cells. Table 4.5 compares the SHJ cell's electrical parameters to other related simulation and experimental references [30, 34, 48]. Meanwhile, Table 4.6 arranges the parameters extracted from the corresponding I-V characteristics for the single top and bottom cells. The results obtained for the PSC exhibit remarkably similar values in terms of efficiency, J_{sc}, V_{oc}, and FF. For the efficiency of SHJ solar cell of single and bottom cells they are found 21.43 % and 8.74 %, respectively, and the J_{sc} of the single and bottom cells are 33.18 mA/cm² and 15.35 mA/cm², respectively. This notable drop in PCE and J_{sc} can be attributed to the absorption of a significant portion of incident light photons within the top cell layers.
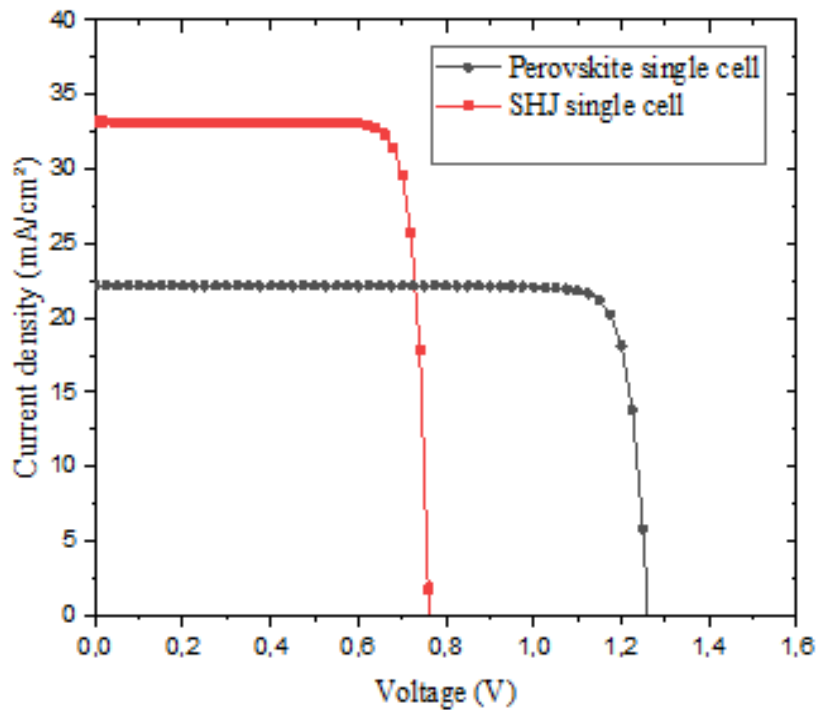
Figure 4.9: Single PVK and single SHJ Current-Voltage curves.

Table 4.5: PV parameters of SHJ single cell compared with reference cells

	V_{oc} (V)	J_{sc} (mA/cm^2)	FF (%)	Efficiency (%)
SHJ single cell	0.76	33.18	84.76	21.43
SHJ single reference cell [30]	0.75	34.7	-	22.05
SHJ single reference cell [34]	0.718	36.5	83.6	21.9
Sanyo's parameters [48]	0.725	38.9	79.1	22.3

61

4.3.2.2 Modelling of the PVK/SHJ tandem solar cell

The schematic structure utilized in this simulation study is presented in Figure 4.6. In this tandem structure we combine Perovskite and SHJ by an interconnection layer of ITO which is positioned between the Spiro-OMeTAD of the top perovskite cell and the amorphous silicon (a-Si) of the bottom SHJ cell. Figure 4.10 displays the I-V characteristic curves for the top, bottom, and tandem solar cells, while Table 4.6 summarizes the output parameters (V_{oc}, J_{sc}, FF and Efficiency) for the perovskite, SHJ, and tandem cells. The obtained results demonstrate that the open-circuit voltage of the tandem Perovskite/SHJ (1.98V) is nearly equal to the sum of the V_{oc} of the sub-cells (1.26 V for the top and 0.71 V for the bottom). The current density of the tandem solar cell (15.38 mA/cm2) is similar to that of the bottom sub-cell (15.35 mA/cm2), implying that the maximum J_{sc} value of the tandem solar cell is dependent on the low J_{sc} of the SHJ bottom sub-cell, which is due to a mismatched current between the top and bottom cells, this is simply due to the mismatched current between the top and the bottom cells. To deal with this fundamental issue, the following section outlines the method employed to achieve a similar photocurrent in both sub-cells.

Figure 4.10: Current-Voltage curves of top, bottom and tandem cells.

Table 4.6: PV parameters of PVK, SHJ and tandem solar cells

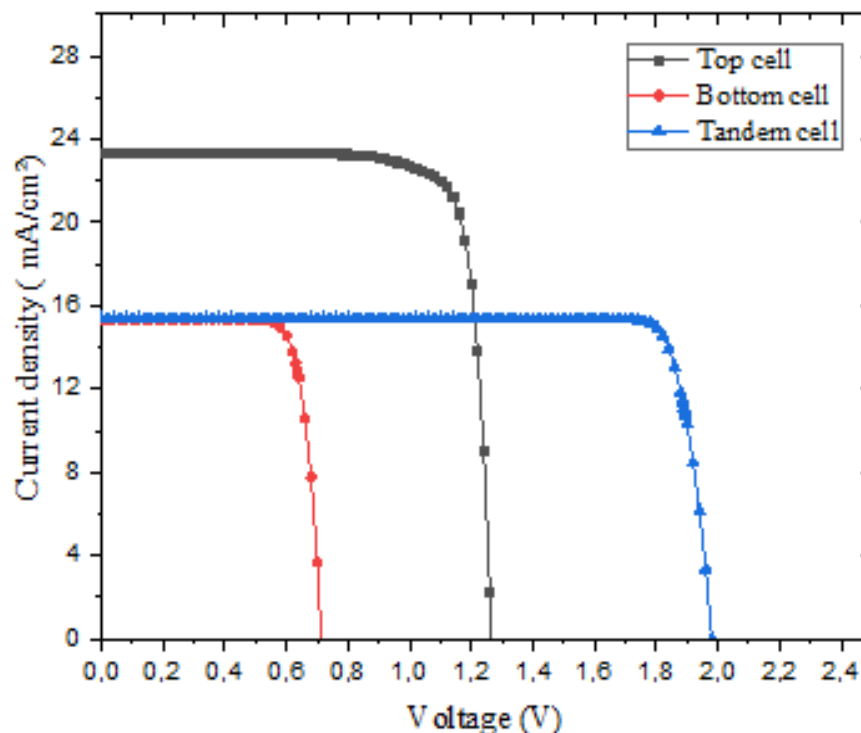|	V_{oc} (V)	J_{sc} (mA/cm^2)	FF (%)	Efficiency (%)
PVK single cell	1.26	22.16	87.27	24.38
PVK top cell	1.26	23.31	82.41	24.33
SHJ single cell	0.76	33.18	84.76	21.43
SHJ bottom cell	0.71	15.35	79.78	8.74
PVK/SHJ tandem cell	1.98	15.38	88.60	27.02

4.3.2.3 Influence of PVK thickness on the tandem cell

Perovskite-on-silicon solar cell have been modelled in this section, in which both sub-cells must be simulated to achieve equivalent current density, a concept known as 'current matching.' Techniques such as adjusting the thickness of the perovskite top cell, enhancing the infrared spectral response, and reducing reflection losses and parasitic absorption [100, 101] are highly effective strategies to achieve current matching. GK Burra and colleagues, utilizing Matlab, optimized tandem cell efficiency by varying the band gap and thickness of the perovskite top solar cell, achieving an impressive PCE of 32% [102].

In this section, we adjusted the perovskite top cell thickness from 0.28 µm to 0.1 µm while maintaining the crystalline-silicon bottom thickness constant at 3 µm, because the sub-cell with lower current density J_{sc} value limits the J_{sc} for the entire tandem cell. Figure 4.11 illustrates the J_{sc} of both top and bottom cells as a function of perovskite thickness variation. It is evident from the figure that as the thickness of the top cell decreases, the J_{sc} of the bottom cell increases, while the J_{sc} of the top cell decreases. This significant difference in J_{sc} arises because the thicker top cell absorbs a greater amount of incident light, resulting in less transmitted light reaching the bottom cell, Conversely, a thinner top cell absorbs fewer photons, allowing more light to transmit to the bottom cell. The point of intersection occurs at a thickness of 0.161 µm, achieving the current matching condition where, $J_{sc\ top} \simeq J_{sc\ bottom} \simeq 18.80$ mA/cm^2.
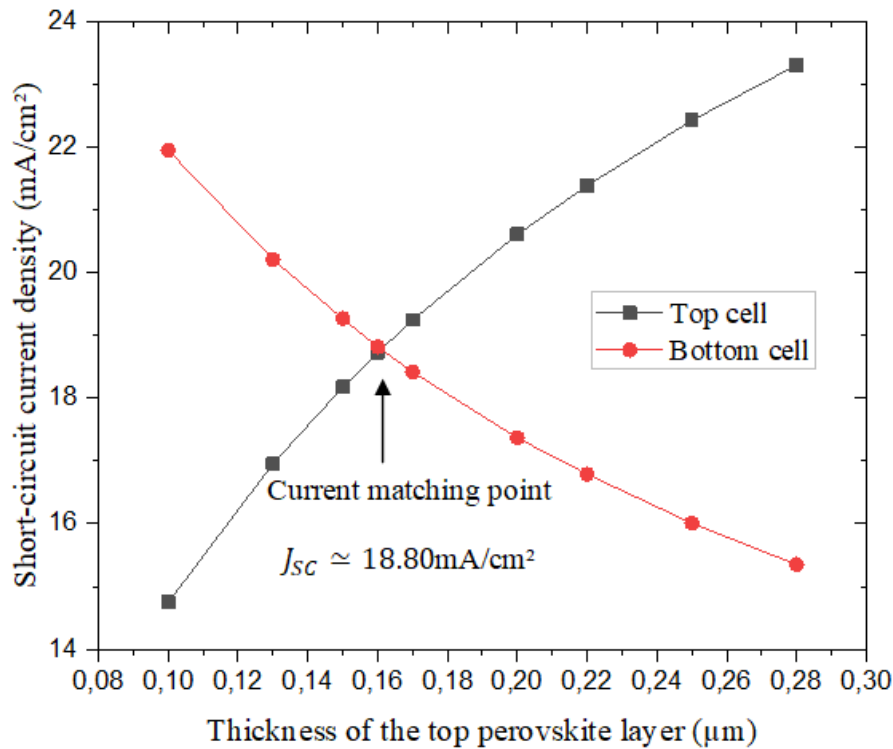
Figure 4.11: Influence of the top cell PVK thickness on the J_{sc} of the two sub-cells.

Figure 4.12 depicts how the thickness of the perovskite layer affects the behaviour of the perovskite/SHJ tandem solar cell In Figure 4.12(a), the open-circuit voltage (V_{oc}) values remain at around 2 V, indicating that changes in the perovskite thickness of the top cell do not significantly impact V_{oc} performance.

Figure 4.12(b) shows that the short-circuit current density (J_{sc}) increases from 15.04 mA/cm² (at 0.1 µm) to a peak value of 18.81 mA/cm² (at 0.161 µm) and then gradually decreases to 15.38 mA/cm². This boost in J_{sc} can be attributed to improved photon absorption in the perovskite top cell. Consequently, by comparing Figure 4.12(b) with Figure 4.11, it becomes evident that at perovskite thicknesses greater than 0.161 µm, the J_{sc} of the tandem cell depends on the J_{sc} of the bottom cell, whereas at perovskite thicknesses less than 0.161 µm, the J_{sc} of the tandem cell relies on J_{sc} of the top cell.

Figure 4.12(c) demonstrates that the fill factor (FF) decreases from 88.72% at a thickness of 0.1 µm to a minimum value of 83.61% at 0.161 µm, then it will rises to 88.6% at 0.28 µm.

In Figure 4.12(d), the power conversion efficiency (PCE) increases as the thickness of the top cell perovskite layer increases, going from 27.25% at 0.1 µm to a peak of 31.67% at the best PVK thickness of 0.161 µm. Subsequently, the PCE decreases to 27.02% at 0.28 µm. It's

noteworthy that the PCE curve follows a similar trend to the current density (J_{sc}) curve presented in Figure 4.12(b).
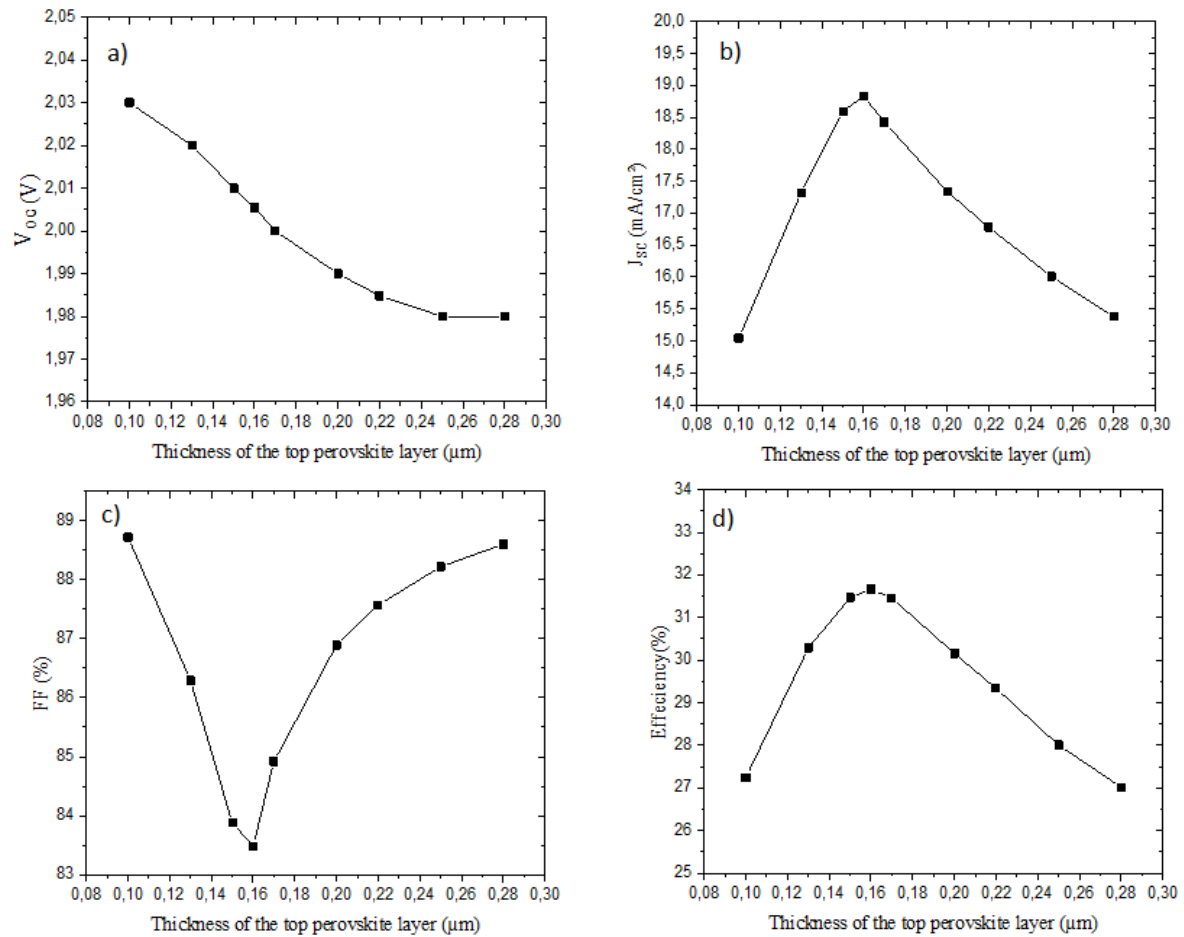
Figure 4.12: Influence of the top cell PVK thickness on different output parameters of the PVK/SHJ tandem solar cell.

Figure 4.13 exhibits the I-V characteristic curves of top, bottom, and tandem solar cells under AM1.5G spectrum illumination, as well as the current matching condition between the cells. The output parameters derived from I-V characteristics are summarized in Table 4.7. The current J_{sc} of the top, bottom, and tandem cells is almost equivalent to 18.80 mA/cm2, whereas the open circuit voltage V_{oc} of the tandem cell (2.01 V) is the sum of the single cell voltages (1.28 V and 0.72 V). The PCE of the PVK/SHJ tandem cell has been increased from 27.02% (Fig. 4.10) to 31.67%
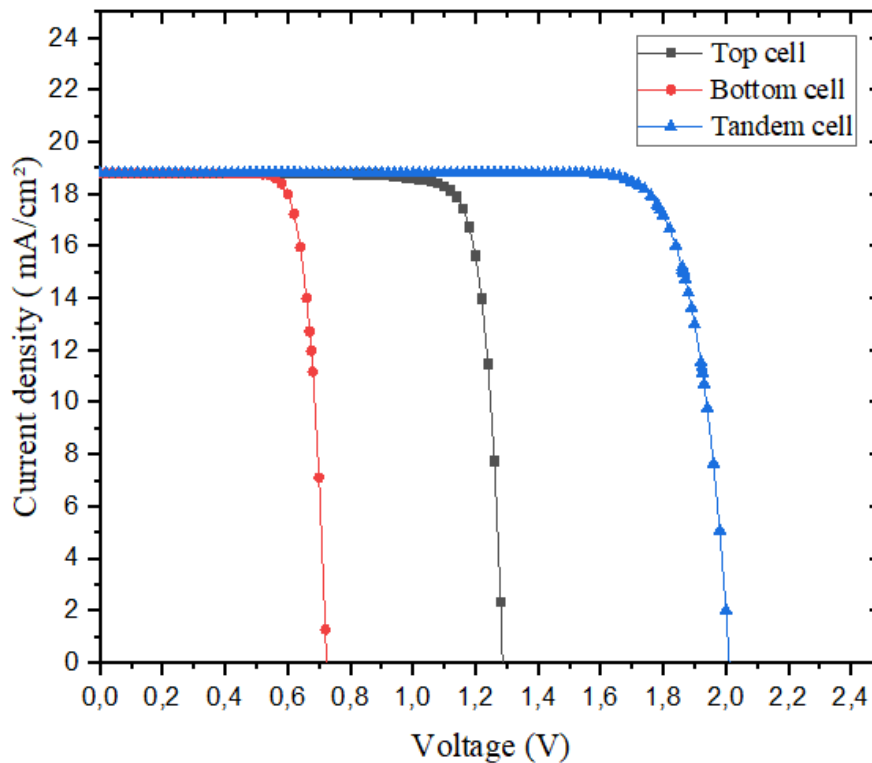
Figure 4.13: I-V Current-Voltage curves of top, bottom and tandem cells.

Table 4.7: Solar cells output parameters.

	V_{oc} (V)	J_{sc} (mA/cm^2)	FF (%)	Efficiency (%)
PVK top cell	1.28	18.79	4.43	20.42
SHJ bottom cell	0.72	18.80	9.41	10.81
PVK/SHJ tandem cell	2.01	18.81	3.61	31.67

External quantum efficiency (EQE) spectra for top and bottom cells with varied perovskite layer thicknesses are shown in Fig. 4.14. The top cell has an EQE maximum about 0.4 µm, whereas the bottom cell has an EQE maximum at 0.9 µm. Short wavelengths less than 0.7 µm are primarily absorbed by the perovskite top cell, while wavelengths between 0.7 µm and 1.1µm are mainly absorbed by the SHJ bottom cell. The bottom cell's EQE performance with a perovskite layer of 161 nm was improved between 0.4 m and 0.8 m, indicating that the two sub-cells were clearly well-matched.
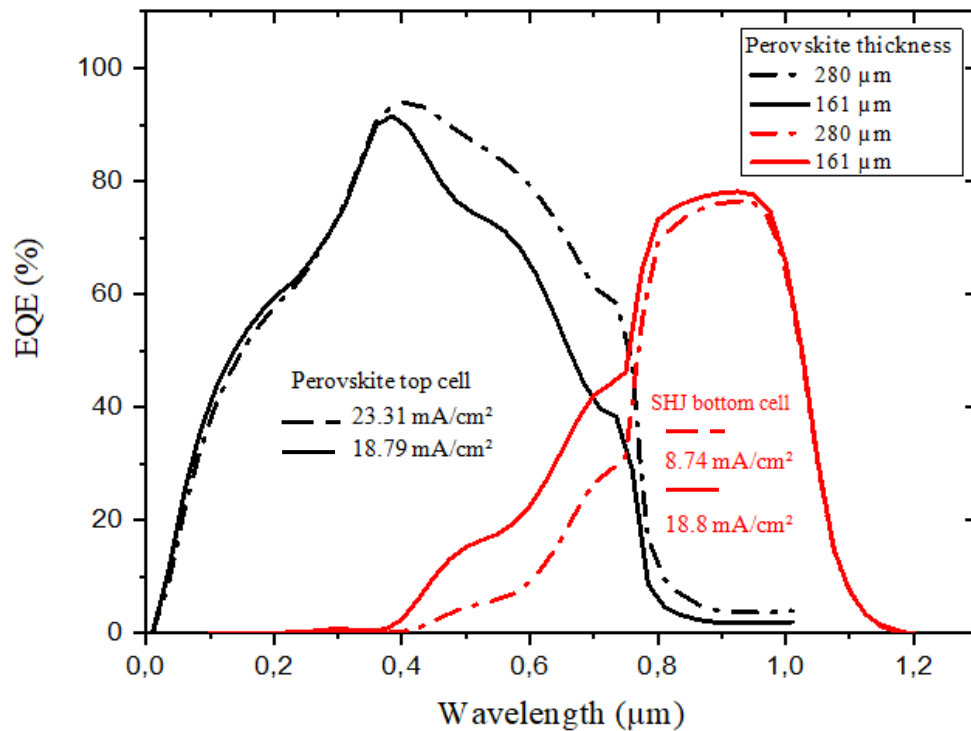
Figure 4.14: Top and bottom external quantum efficiency in tandem device.

4.4 Conclusion

In the first part of this chapter, the performance of $CH_3NH_3PbI_{3-x}Br_x$ perovskite solar cell was simulated and investigated as a function of different layers thickness of the structure $TiO_2/CH_3NH_3PbI_{3-x}Br_x$/Spiro-OMeTADOur simulation results reveal a remarkable impact of the perovskite layer when compared to the ETL and HTL layers. By optimizing the thicknesses of the perovskite structure to 100 nm for TiO_2, 100 nm for Spiro-OMeTAD, and 400 nm for $CH_3NH_3PbI_{3-x}Br_x$, we achieve the highest power conversion efficiency (PCE) of 20.35%. This PCE value has further been enhanced to 24.72% by considering a longer carrier lifetime. Notably, the simulated results closely match experimental data presented in the literature. While for the second part, we designed Perovskite/Silicon tandem solar cell structure where $CH_3NH_3PbI_{3-x}Br_x$ and Silicon-hetero-junction (SHJ) are top and bottom cells, respectively. We have firstly simulated the single perovskite and single silicon cells and compare the results to other simulated and experimental results. Furthermore, we have simulated the tandem cell structure revealing a current mismatch between the two sub-cells. We modified the thickness of the perovskite top cell at the end of this section to improve tandem cell efficiency and accomplish the current matching condition between the cells. The simulation outcomes

demonstrate a performance enhancement of the PVK/SHJ tandem cell, resulting in a remarkable PCE of 31.67%.

Conclusion

Conclusion

Perovskite/silicon tandem solar cells have attracted significant research interest in recent years due to their potential to improve the efficiency and stability of photovoltaic devices. Perovskite materials have recently emerged as a promising option for use in tandem solar cells, due to their high absorption coefficients and tunable bandgaps, which can be optimized to match the solar spectrum. On the other hand, Silicon bottom solar cells are often used as the bottom layer in perovskite tandem solar cells. This is because silicon has a bandgap of 1.1 eV, which allows it to efficiently convert photons in the visible portion of the solar spectrum. Our work was divided into two parts; the first part investigates a single junction solar cell based on methylammonium mixed bromide iodide lead perovskite $CH_3NH_3PbI_{3-x}Br_x$, where the PVK region is stuck between ETL and a HTL. The obtained results of this structure were compared to a similar experimental design and then optimized by improving the layer thicknesses of the perovskite, ETL and HTL. After achieving good power conversion efficiency (PCE) of 20.35%, we have also improved this PCE to 24.72% taking into account a longer carrier life time.

In the second part, we have modelled perovkite/silicon heterojunction SHJ tandem solar cell under AM1.5 light spectrum. Where the perovskite top cell structure consists of $TiO_2/CH_3NH_3PbI_{3-x}Br_x$/Spiro-OMeTAD, while for the SHJ cell, it comprises of n-a-Si/i-a-Si/n-c-Si/i-a-Si/p-a-Si. We begin our simulated work by individually modelled the single top and single bottom with efficiency of 24.38% and 21.43%, respectively. The efficiency of the Perovskite/SHJ tandem structure was determined to be 27.02% under mismatched current densities. Finally, we investigated the impact of the thickness of the perovskite top cell on the performance of the tandem cell, aiming to enhance the power conversion efficiency (PCE). The results indicate a peak PCE of 31.67% at an optimal thickness of 0.161 μm. This represents the achievement of a current matching condition where the current densities of the top, bottom, and tandem cells are approximately equal, Jsc top $\simeq$ Jsc bottom $\simeq$ Jsc tandem $\simeq$ 18.80 mA/cm2.

Recent perovskite solar cells are becoming increasingly cost and performance competitive with silicon technology. They offer a variety of materials, structures, and straightforward processing techniques, resulting in interesting properties that are compatible with different solar cell applications, whether in a simple or tandem configuration. As a future perspective, solar cells based on perovskite can be configured with different cations based on cesium (Cs) or Formamidinium (FA). Or with other material combination; mixed hadile or mixed cation perovskite. Finally, the perovskite-based solar cell brings new promise and inspiration to solar cells and their applications due to its tunable bandgap and high absorption coefficients and hence high power conversion efficiency.

Bibliography

Bibliography

[1] Green, M. A., Ho-Baillie, A., & Snaith, H. J. (2014). The emergence of perovskite solar cells. *Nature photonics*, *8*(7), 506-514.

[2] Snaith, H. J. (2013). Perovskites: the emergence of a new era for low-cost, high-efficiency solar cells. *The journal of physical chemistry letters*, *4*(21), 3623-3630.

[3] Kim, C. U., Yu, J. C., Jung, E. D., Choi, I. Y., Park, W., Lee, H., ... & Choi, K. J. (2019). Optimization of device design for low cost and high efficiency planar monolithic perovskite/silicon tandem solar cells. *Nano Energy*, *60*, 213-221.

[4] Elbar, M., Tobbeche, S., & Merazga, A. (2015). Effect of top-cell CGS thickness on the performance of CGS/CIGS tandem solar cell. *Solar energy*, *122*, 104-112.

[5] Benaicha, M., Dehimi, L., Pezzimenti, F., & Bouzid, F. (2020). Simulation analysis of a high efficiency GaInP/Si multijunction solar cell. *Journal of Semiconductors*, *41*(3), 032701.

[6] Jacobsson, T. J., Hultqvist, A., Svanström, S., Riekehr, L., Cappel, U. B., Unger, E., ... & Boschloo, G. (2020). 2-Terminal CIGS-perovskite tandem cells: A layer by layer exploration. *Solar Energy*, *207*, 270-288.

[7] Shivarudraiah, S. B., Ng, M., Li, C. H. A., & Halpert, J. E. (2020). All-Inorganic, Solution-Processed, Inverted CsPbI3 Quantum Dot Solar Cells with a PCE of 13.1% Achieved via a Layer-by-Layer FAI Treatment. *ACS Applied Energy Materials*, *3*(6), 5620-5627.

[8] Todorov, T., Gershon, T., Gunawan, O., Lee, Y. S., Sturdevant, C., Chang, L. Y., & Guha, S. (2015). Monolithic perovskite-CIGS tandem solar cells via in situ band gap engineering. *Advanced Energy Materials*, *5*(23), 1500799.

[9] Madan, J., Pandey, R., & Sharma, R. (2020). Device simulation of 17.3% efficient lead-free all-perovskite tandem solar cell. *Solar Energy*, *197*, 212-221.

[10] Eperon, G. E., Leijtens, T., Bush, K. A., Prasanna, R., Green, T., Wang, J. T. W., ... & Snaith, H. J. (2016). Perovskite-perovskite tandem photovoltaics with optimized band gaps. *Science*, *354*(6314), 861-865.

[11] Forgács, D., Gil-Escrig, L., Pérez-Del-Rey, D., Momblona, C., Werner, J., Niesen, B., ... & Bolink, H. J. (2017). Efficient monolithic perovskite/perovskite tandem solar cells. *Advanced Energy Materials*, *7*(8), 1602121.

[12] Hossain, M. I., Saleque, A. M., Ahmed, S., Saidjafarzoda, I., Shahiduzzaman, M., Qarony, W., ... & Tsang, Y. H. (2021). Perovskite/perovskite planar tandem solar cells: A comprehensive guideline for reaching energy conversion efficiency beyond 30%. *Nano Energy*, *79*, 105400.

[13] Pandey, R., Singla, A., Madan, J., Sharma, R., & Chaujar, R. (2019). Toward the design of monolithic 23.1% efficient hysteresis and moisture free perovskite/c-Si HJ tandem solar cell: a numerical simulation study. *Journal of Micromechanics and Microengineering*, *29*(6), 064001.

[14] De Bastiani, M., Mirabelli, A. J., Hou, Y., Gota, F., Aydin, E., Allen, T. G., ... & De Wolf, S. (2021). Efficient bifacial monolithic perovskite/silicon tandem solar cells via bandgap engineering. *Nature Energy*, *6*(2), 167-175.

[15] Yang, D., Zhang, X., Hou, Y., Wang, K., Ye, T., Yoon, J., ... & Priya, S. (2021). 28.3%-efficiency perovskite/silicon tandem solar cell by optimal transparent electrode for high efficient semitransparent top cell. *Nano Energy*, *84*, 105934.

[16] Pandey, R., & Chaujar, R. (2016). Numerical simulations: Toward the design of 27.6% efficient four-terminal semi-transparent perovskite/SiC passivated rear contact silicon tandem solar cell. *Superlattices and Microstructures*, *100*, 656-666.

[17] Gharibzadeh, S., Hossain, I. M., Fassl, P., Nejand, B. A., Abzieher, T., Schultes, M., ... & Paetzold, U. W. (2020). 2D/3D heterostructure for semitransparent perovskite solar cells with engineered bandgap enables efficiencies exceeding 25% in four-terminal tandems with silicon and CIGS. *Advanced Functional Materials*, *30*(19), 1909919.

[18] Filipič, M., Löper, P., Niesen, B., De Wolf, S., Krč, J., Ballif, C., & Topič, M. (2015). CH 3 NH 3 PbI 3 perovskite/silicon tandem solar cells: characterization based optical simulations. *Optics express*, *23*(7), A263-A278.

[19] Huang, H., Tian, G., Zhou, L., Yuan, J., Fahrner, W. R., Zhang, W., ... & Liu, R. (2018). Simulation and experimental study of a novel bifacial structure of silicon heterojunction solar cell for high efficiency and low cost. *Chinese Physics B*, *27*(3), 038502.

[20] Kanevce, A., & Metzger, W. K. (2009). The role of amorphous silicon and tunneling in heterojunction with intrinsic thin layer (HIT) solar cells. *Journal of Applied Physics*, *105*(9), 094507.

[21] Mehmood, H., Nasser, H., Özkol, E., Tauqeer, T., Hussain, S., & Turan, R. (2017, August). Physical device simulation of partial dopant-free asymmetric silicon heterostructure solar cell (P-DASH) based on hole-selective molybdenum oxide (MoOx) with crystalline silicon (cSi). In *2017 International Conference on Engineering and Technology (ICET)* (pp. 1-6). IEEE.

[22] Hsu, C. H., Zhang, X. Y., Lin, H. J., Lien, S. Y., Cho, Y. S., & Ye, C. S. (2019). Numerical simulation of crystalline silicon heterojunction solar cells with different p-type a-SiOx window layer. *Energies*, *12*(13), 2541.

[23] Hayashi, Y., Li, D., Ogura, A., & Ohshita, Y. (2013). Role of i-aSi: H layers in aSi: H/cSi heterojunction solar cells. *IEEE Journal of Photovoltaics*, *3*(4), 1149-1155.

[24] Dong, G., Hong, C., Cui, G., Long, W., Lu, H., Lan, T., ... & Xu, X. (2018, June). Water Vapor Doped TCO Films and Application to Silicon Heterojunction Solar Cells. In *2018 IEEE 7th World Conference on Photovoltaic Energy Conversion (WCPEC)(A Joint Conference of 45th IEEE PVSC, 28th PVSEC & 34th EU PVSEC)* (pp. 2121-2125). IEEE.

[25] Green, M. A., Ho-Baillie, A., & Snaith, H. J. (2014). The emergence of perovskite solar cells. *Nature photonics*, *8*(7), 506-514.

[26] Snaith, H. J. (2013). Perovskites: the emergence of a new era for low-cost, high-efficiency solar cells. *The journal of physical chemistry letters*, *4*(21), 3623-3630.

[27] Kim, C. U., Yu, J. C., Jung, E. D., Choi, I. Y., Park, W., Lee, H., ... & Choi, K. J. (2019). Optimization of device design for low cost and high efficiency planar monolithic perovskite/silicon tandem solar cells. *Nano Energy*, *60*, 213-221.

[28] Cho, H., Jeong, S. H., Park, M. H., Kim, Y. H., Wolf, C., Lee, C. L., ... & Lee, T. W. (2015). Overcoming the electroluminescence efficiency limitations of perovskite light-emitting diodes. *Science*, *350*(6265), 1222-1225.

[29] Zhu, H., Fu, Y., Meng, F., Wu, X., Gong, Z., Ding, Q., ... & Zhu, X. Y. (2015). Lead halide perovskite nanowire lasers with low lasing thresholds and high quality factors. *Nature materials*, *14*(6), 636-642.

[30] Stranks, S. D., & Snaith, H. J. (2015). Metal-halide perovskites for photovoltaic and light-emitting devices. *Nature nanotechnology*, *10*(5), 391-402.

[31] Tan, Z. K., Moghaddam, R. S., Lai, M. L., Docampo, P., Higler, R., Deschler, F., ... & Friend, R. H. (2014). Bright light-emitting diodes based on organometal halide perovskite. *Nature nanotechnology*, *9*(9), 687-692.

[32] Tang, L., Peng, Y., Zhou, Z., Wu, Y., Xu, J., Li, J., ... & Zhang, J. (2018). High-performance organic–inorganic hybrid perovskite thin-film field-effect transistors. *Applied Physics A*, *124*(9), 624.

[33] Ji, J., Haque, F., Hoang, N. T. T., & Mativenga, M. (2019). Ambipolar Transport in Methylammonium Lead Iodide Thin Film Transistors. *Crystals*, *9*(10), 539.

[34] Chin, X. Y., Cortecchia, D., Yin, J., Bruno, A., & Soci, C. (2015). Lead iodide perovskite light-emitting field-effect transistor. *Nature communications*, *6*, 7383.

[35] Kojima, A., Teshima, K., Shirai, Y., & Miyasaka, T. (2009). Organometal halide perovskites as visible-light sensitizers for photovoltaic cells. *Journal of the American Chemical Society*, *131*(17), 6050-6051.

[36] Jeon, N. J., Noh, J. H., Yang, W. S., Kim, Y. C., Ryu, S., Seo, J., & Seok, S. I. (2015). Compositional engineering of perovskite materials for high-performance solar cells. *Nature*, *517*(7535), 476-480.

[37] Lee, M. M., Teuscher, J., Miyasaka, T., Murakami, T. N., & Snaith, H. J. (2012). Efficient hybrid solar cells based on meso-superstructured organometal halide perovskites. *Science*, *338*(6107), 643-647.

[38] Zheng, X., Hou, Y., Bao, C., Yin, J., Yuan, F., Huang, Z., ... & Bakr, O. M. (2020). Managing grains and interfaces via ligand anchoring enables 22.3%-efficiency inverted perovskite solar cells. *Nature Energy*, *5*(2), 131-140.

[39] Jeong, M., Choi, I. W., Go, E. M., Cho, Y., Kim, M., Lee, B., ... & Yang, C. (2020). Stable perovskite solar cells with efficiency exceeding 24.8% and 0.3-V voltage loss. *Science*, *369*(6511), 1615-1620.

[40] Yang, W. S., Noh, J. H., Jeon, N. J., Kim, Y. C., Ryu, S., Seo, J., & Seok, S. I. (2015). High-performance photovoltaic perovskite layers fabricated through intramolecular exchange. *Science*, *348*(6240), 1234-1237.

[41] Green, M. A. (2017). Corrigendum to 'Solar cell efficiency tables (version 49)'[Prog. Photovolt: Res. Appl. 2017; 25: 3–13]. *Progress in Photovoltaics: Research and Applications*, *25*(4), 333-334.

[42] NREL, Best Research-Cell Efficiencies, https://www.nrel.gov/pv/assets/pdfs/best-research-cell-efficiencies.20200104.pdf.

[43] Stranks, S. D., Eperon, G. E., Grancini, G., Menelaou, C., Alcocer, M. J., Leijtens, T., ... & Snaith, H. J. (2013). Electron-hole diffusion lengths exceeding 1 micrometer in an organometal trihalide perovskite absorber. *Science*, *342*(6156), 341-344.

[44] Noh, J. H., Im, S. H., Heo, J. H., Mandal, T. N., & Seok, S. I. (2013). Chemical management for colorful, efficient, and stable inorganic–organic hybrid nanostructured solar cells. *Nano letters*, *13*(4), 1764-1769.

[45] Unger, E. L., Kegelmann, L., Suchan, K., Sörell, D., Korte, L., & Albrecht, S. (2017). Correction: Roadmap and roadblocks for the band gap tunability of metal halide perovskites. *Journal of Materials Chemistry A*, *5*(30), 15983-15983.

[46] Eperon, G. E., Stranks, S. D., Menelaou, C., Johnston, M. B., Herz, L. M., & Snaith, H. J. (2014). Formamidinium lead trihalide: a broadly tunable perovskite for efficient planar heterojunction solar cells. *Energy & Environmental Science*, *7*(3), 982-988.

[47] Sutton, R. J., Eperon, G. E., Miranda, L., Parrott, E. S., Kamino, B. A., Patel, J. B., ... & Snaith, H. J. (2016). Bandgap-tunable cesium lead halide perovskites with high thermal stability for efficient solar cells. *Advanced Energy Materials*, *6*(8), 1502458.

[48] Sun, S., Salim, T., Mathews, N., Duchamp, M., Boothroyd, C., Xing, G., ... & Lam, Y. M. (2014). The origin of high efficiency in low-temperature solution-processable bilayer organometal halide hybrid solar cells. *Energy & Environmental Science*, *7*(1), 399-407.

[49] Wehrenfennig, C., Liu, M., Snaith, H. J., Johnston, M. B., & Herz, L. M. (2014). Homogeneous emission line broadening in the organo lead halide perovskite ch3nh3pbi3–x cl x. *The journal of physical chemistry letters*, *5*(8), 1300-1306.

[50] Hima, A., Lakhdar, N., Benhaoua, B., Saadoune, A., Kemerchou, I., & Rogti, F. (2019). An optimized perovskite solar cell designs for high conversion efficiency. *Superlattices and Microstructures*, *129*, 240-246.

[51] Hima, A., Khechekhouche, A., Kemerchou, I., Lakhdar, N., Benhaoua, B., Rogti, F., ... & Saadoun, A. (2018). GPVDM simulation of layer thickness effect on power conversion efficiency of CH3NH3PbI3 based planar heterojunction solar cell. *International Journal of Energetica*, *3*(1), 37-41.

[52] Azri, F., Meftah, A., Sengouga, N., & Meftah, A. (2019). Electron and hole transport layers optimization by numerical simulation of a perovskite solar cell. *Solar Energy*, *181*, 372-378.

[53] Jeon, N. J., Noh, J. H., Kim, Y. C., Yang, W. S., Ryu, S., & Seok, S. I. (2014). Solvent engineering for high-performance inorganic–organic hybrid perovskite solar cells. N0ature materials, 13(9), 897-903.

[54] S. M. Sze, Semiconductor Devices, 2nd edition, John Wiley & Sons, Inc, 2001.

[55] Gelinas, R. (2005). *A novel approach to modeling tunnel junction diodes using Silvaco ATLAS software*. NAVAL POSTGRADUATE SCHOOL MONTEREY CA.

[56] Fotis, K. (2012). *Modeling and simulation of a dual-junction CIGS solar cell using Silvaco ATLAS*. NAVAL POSTGRADUATE SCHOOL MONTEREY CA.

[57] Garcia, B. (2007). *Indium gallium nitride multijunction solar cell simulation using silvaco atlas* (Doctoral dissertation, Monterey California. Naval Postgraduate School).

[58] Hossain, M. J. (2016). *Novel high efficiency quadruple junction solar cell with current matching and optimized quantum efficiency* (Doctoral dissertation, Tennessee Technological University).

[59] Schiavo, D. (2012). *Modeling Radiation Effects on a Triple Junction Solar Cell using Silvaco ATLAS*. NAVAL POSTGRADUATE SCHOOL MONTEREY CA.

[60] Fell, A., Niewelt, T., Steinhauser, B., Heinz, F. D., Schubert, M. C., & Glunz, S. W. (2021). *Radiative recombination in silicon photovoltaics: Modeling the influence of charge carrier densities and photon recycling. Solar Energy Materials and Solar Cells, 230, 111198.*

[61] Werner, J. (2018). *Perovskite/Silicon Tandem Solar Cells: Toward Affordable Ultra-High Efficiency Photovoltaics?* (No. THESIS). EPFL.

[62] McMeekin, D. P., et al. (2016). A mixed-cation lead mixed-halide perovskite absorber for tandem solar cells. Science, 351(6269), 151-155.

[63] Zheng, X., et al. (2020). Mixed Halide Perovskites for Tandem Solar Cells: Stability, Optoelectronic Properties, and Interface Engineering. Advanced Energy Materials, 10(18), 1903627.

[64] Yin, Z., Lu, B., Chen, Y., & Guo, C. (2022). Advances of Commercial and Biological Materials for Electron Transport Layers in Biological Applications. *Frontiers in Bioengineering and Biotechnology*, 968.

[65] Singh, A., Verma, U. K., & Tonk, A. Device structures of Perovskite solar cells: A critical review. *physica status solidi (a)*.

[66] Li, S., Cao, Y. L., Li, W. H., & Bo, Z. S. (2021). A brief review of hole transporting materials commonly used in perovskite solar cells. *Rare Metals*, *40*(10), 2712-2729.

[67] Song, Z., Watthage, S. C., Phillips, A. B., & Heben, M. J. (2016). Pathways toward high-performance perovskite solar cells: review of recent advances in organo-metal halide perovskites for photovoltaic applications. *Journal of photonics for energy*, *6*(2), 022001-022001.

[68] Mali, S. S., & Hong, C. K. (2016). pin/nip type planar hybrid structure of highly efficient perovskite solar cells towards improved air stability: synthetic strategies and the role of p-type hole transport layer (HTL) and n-type electron transport layer (ETL) metal oxides. *Nanoscale*, *8*(20), 10528-10540.

[69] Yu, H. J., Xiao, J., Chen, J., Ren, X., Qi, Y. E., Min, X., & Shao, G. (2023). Synthesis, Properties, and Application of Small-Molecule Hole-Transporting Materials Based on Acetylene-Linked Thiophene Core. *Molecules*, *28*(9), 3739.

[70] National Renewable Energy Laboratory (NREL), "Best Research-Cell Efficiency Chart," accessed April 2023

[71] National Renewable Energy Laboratory (NREL), "Perovskite Solar Cells: Low Cost, High Efficiency," accessed April 2023

[72] M. Saliba et al., "A molecularly engineered hole-transporting material for efficient perovskite solar cells," Nature Energy, vol. 1, no. 10, pp. 1-8, Sep. 2016

[73] A. Abate et al., "Perovskite solar cells on plastic substrates: from stability to degradation mechanisms," Solid State Energy, vol. 129, pp. 140-148, Nov. 2016

[74] H. Zhou et al., "Progress of perovskite solar cells in the past decade: Efficiency, stability and practical application," Journal of Materials Chemistry A, vol. 9, no. 4, pp. 1704-1745, Jan. 2021

[75] Laalioui, S. (2022). Perovskite-Based Solar Cells. In *Perovskite-Based Solar Cells*. De Gruyter.

[76] K. Masuko et al., "Achievement of more than 25% conversion efficiency with crystalline silicon heterojunction solar cell," IEEE J. Photovoltaics, vol. 4, no. 6, pp. 1433–1435,2014,doi:10.1109/JPHOTOV.2014.2352151.

[77] M. Taguchi et al., "24.7% Record efficiency HIT solar cell on thin silicon wafer," IEEEJ.Photovoltaics,vol.4,no.1,pp.96–99,2014,doi:10.1109/JPHOTOV.2013.2282737.

[78] K. Yoshikawa et al., "Silicon heterojunction solar cell with interdigitated back contacts for a photoconversion efficiency over 26%," Nat. Energy, vol. 2, no. 5, p. 17032, 2017, doi:10.1038/nenergy.2017.32.

[79] "best-research-cell-efficiencies.20200803.pdf."2020,[Online].Available: https://www.nrel.gov/pv/assets/images/efficiency-chart.png.

[80] Löper, P., Moon, S. J., De Nicolas, S. M., Niesen, B., Ledinsky, M., Nicolay, S., ... & Ballif, C. (2015). Organic–inorganic halide perovskite/crystalline silicon four-terminal tandem solar cells. *Physical Chemistry Chemical Physics*, *17*(3), 1619-1629.

[81] Bailie, C. D., Christoforo, M. G., Mailoa, J. P., Bowring, A. R., Unger, E. L., Nguyen, W. H., ... & McGehee, M. D. (2015). Semi-transparent perovskite solar cells for tandems with silicon and CIGS. *Energy & Environmental Science*, *8*(3), 956-963.

[82] M. Filipič, P. Löper, B. Niesen, S. De Wolf, J. Krč, C. Ballif, and M. Topič, "Ch 3 nh 3 pbi 3 perovskite/silicon tandem solar cells: characterization based optical simulations," Optics express 23, A263–A278 (2015).

[83] B. W. Schneider, N. N. Lal, S. Baker-Finch, and T. P. White, "Pyramidal surface textures for light trapping and antireflection in perovskite-on-silicon tandem solar cells," Optics express 22, A1422–A1430 (2014).

[84] Kranz, L., Abate, A., Feurer, T., Fu, F., Avancini, E., Löckinger, J., ... & Tiwari, A. N. (2015). High-efficiency polycrystalline thin film tandem solar cells. *The journal of physical chemistry letters*, *6*(14), 2676-2681.

[85] Werner, J., Weng, C. H., Walter, A., Fesquet, L., Seif, J. P., De Wolf, S., ... & Ballif, C. (2016). Efficient monolithic perovskite/silicon tandem solar cell with cell area> 1 cm2. *The journal of physical chemistry letters*, *7*(1), 161-166.

[86] Sullivan, B. P. (2010). *The effect of temperature on the optimization of photovoltaic cells using Silvaco ATLAS modeling*. NAVAL POSTGRADUATE SCHOOL MONTEREY CA.

[87] Bates, A. D. (2004). *Novel optimization techniques for multijunction solar cell design using Silvaco Atlas* (Doctoral dissertation, Master's Thesis, Naval Postgraduate School, Monterey, California).

[88] Tu, Y., Wu, J., Lan, Z., He, X., Dong, J., Jia, J., ... & Huang, Y. (2017). Modulated CH3NH3PbI3−xBrx film for efficient perovskite solar cells exceeding 18%. *Scientific reports*, *7*(1), 1-8.

[89] Tavakoli, M. M., Yadav, P., Tavakoli, R., & Kong, J. (2018). Surface engineering of TiO2 ETL for highly efficient and hysteresis-less planar perovskite solar cell (21.4%) with enhanced open-circuit voltage and stability. *Advanced Energy Materials*, *8*(23), 1800794.

[90] Lee, J. W., Kim, H. S., & Park, N. G. (2016). Lewis acid–base adduct approach for high efficiency perovskite solar cells. *Accounts of chemical research*, *49*(2), 311-319.

[91] Hima, A., Lakhdar, N., Benhaoua, B., Saadoune, A., Kemerchou, I., & Rogti, F. (2019). An optimized perovskite solar cell designs for high conversion efficiency. *Superlattices and Microstructures*, *129*, 240-246.

[92] Rolland, A., Pedesseau, L., Kepenekian, M., Katan, C., Huang, Y., Wang, S., ... & Even, J. (2018). Computational analysis of hybrid perovskite on silicon 2-T tandem solar cells based on a Si tunnel junction. Optical and Quantum Electronics, 50(1), 21.

[93] Bacha, M., Saadoune, A., & Youcef, I. (2021). Numerical simulation and optimization of CH3NH3PbI3− xBrx perovskite solar cell for high conversion efficiency. *Optical Materials*, *122*, 111734.

[94] Cherif, F. E., & Sammouda, H. (2020). Strategies for high performance perovskite/c-Si tandem solar cells: Effects of bandgap engineering, solar concentration and device temperature. *Optical Materials*, *106*, 109935.

[95] Kanevce, A., & Metzger, W. K. (2009). The role of amorphous silicon and tunneling in heterojunction with intrinsic thin layer (HIT) solar cells. *Journal of Applied Physics*, *105*(9), 094507.

[96] Taira, S., Yoshimine, Y., Baba, T., Taguchi, M., Kinoshita, T., Sakata, H., ... & Tanaka, M. (2007). to be published in Proc. 22nd European Photovoltaic Solar Energy Conf. *Exhib., Milan*.

[97] Martin A. Green, 'Self-consistent optical parameters of intrinsic silicon at 300 K including temperature coefficients', *Solar Energy Materials and Solar Cells* 92(11), pp.1305-1310, (2008)

[98] Leguy, A. M., Hu, Y., Campoy-Quiles, M., Alonso, M. I., Weber, O. J., Azarhoosh, P., ... & Barnes, P. R. (2015). Reversible hydration of CH3NH3PbI3 in films, single crystals, and solar cells. *Chemistry of Materials*, *27*(9), 3397-3407.

[99] Zachary C. Holman, Antoine Descoeudres, Loris Barraud, Fernando Zicarelli Fernandez, Johannes P. Seif, Stefaan De Wolf and Christophe Ballif, 'Current Losses at the Front of Silicon Heterojunction Solar Cells', *IEEE Journal of Photovoltaics* **2**(1), pp.7-15, (2012)

[100] Richter, A., Hermle, M., & Glunz, S. W. (2013). Reassessment of the limiting efficiency for crystalline silicon solar cells. *IEEE journal of photovoltaics*, *3*(4), 1184-1191.

[101] Jäger, K., Korte, L., Rech, B., & Albrecht, S. (2017). Numerical optical optimization of smonolithic planar perovskite-silicon tandem solar cells with regular and inverted device architectures. *Optics express*, *25*(12), A473-A482.

[102] Burra, G. K., Ghosh, D. S., & Tiwari, S. (2021). Device Simulation of Perovskite/Silicon Tandem Solar Cell with Antireflective Coating.

Scientific Productions

Publications in journals

- **Bacha**, **M.,** Saadoune, A., & Youcef, I. (2021). Numerical simulation and optimization of CH3NH3PbI3− xBrx perovskite solar cell for high conversion efficiency. *Optical Materials*, *122*, 111734.

- **Bacha, M.,** Saadoune, A., & Youcef, I. (2022). Design and numerical investigation of Perovskite/Silicon tandem solar cell. *Optical Materials*, *131*, 112671.

International communication

- 1st International Conference on Sustainable Energy and Advanced Materials IC-SEAM'21 April 21-22, 2021, Ouargla, ALGERIA
  Title: Influence of absorber layer thickness on the performance of perovskite solar cells by Silvaco Atlas simulator
  Authors: Madjda Bacha, Saadoune Achour.

- 8th International Conference on Materials Science and Nanotechnology For next Generation MSNG 2021 14-16 July, 20121, Turkey.
  Title: Effect of absorber layer thickness on the performance of perovskite solar cells by Silvaco Software.
  Authors: Madjda Bacha, Saadoune Achour.

National communication

- 1st National Conference Of Materials Sciences And Renewable Energy CMSRE23 on November 22-23, 2023 in Relizane, Algeria.
  Title: Influence of top cell perovskite thickness on the performance of perovskite/Silicon tandem solar cell.
  Authors: Madjda Bacha, Achour Saadoune, Imad Youcef, Marah Bacha.